Downloaded from http://rsif.royalsocietypublishing.org/ on February 7, 2018

INTERFACE

rsif.royalsocietypublishing.org

Research

Cite this article: Domel AG, Saadat M, Weaver JC, Haj-Hariri H, Bertoldi K, Lauder GV. 2018 Shark skin-inspired designs that improve aerodynamic performance. *J. R. Soc. Interface* **15**: 20170828.
http://dx.doi.org/10.1098/rsif.2017.0828

Received: 3 November 2017
Accepted: 17 January 2018

Subject Category:
Life Sciences–Engineering interface

Subject Areas:
biomimetics, biomechanics

Keywords:
shark skin, denticle, aerofoil, hydrodynamics, lift, vortex generator

Authors for correspondence:
Katia Bertoldi
e-mail: bertoldi@seas.harvard.edu
George V. Lauder
e-mail: glauder@oeb.harvard.edu

†These authors contributed equally to this work.
‡Co-principal investigators.

Electronic supplementary material is available online at https://dx.doi.org/10.6084/m9.figshare.c.3986802.v3.

THE ROYAL SOCIETY PUBLISHING

Shark skin-inspired designs that improve aerodynamic performance

August G. Domel[1,†], Mehdi Saadat[2,4,†], James C. Weaver[3], Hossein Haj-Hariri[4], Katia Bertoldi[1,‡] and George V. Lauder[2,‡]

[1]Harvard University John A. Paulson School of Engineering and Applied Sciences, Cambridge, MA 02138, USA
[2]Department of Organismal and Evolutionary Biology, Harvard University, Cambridge, MA 02138, USA
[3]Wyss Institute for Biologically Inspired Engineering, Cambridge, MA 02138, USA
[4]College of Engineering and Computing, University of South Carolina, Columbia, SC 29208, USA

AGD, 0000-0001-6161-5840

There have been significant efforts recently aimed at improving the aerodynamic performance of aerofoils through the modification of their surfaces. Inspired by the drag-reducing properties of the tooth-like denticles that cover the skin of sharks, we describe here experimental and simulation-based investigations into the aerodynamic effects of novel denticle-inspired designs placed along the suction side of an aerofoil. Through parametric modelling to query a wide range of different designs, we discovered a set of denticle-inspired surface structures that achieve simultaneous drag reduction and lift generation on an aerofoil, resulting in lift-to-drag ratio improvements comparable to the best-reported for traditional low-profile vortex generators and even outperforming these existing designs at low angles of attack with improvements of up to 323%. Such behaviour is enabled by two concurrent mechanisms: (i) a separation bubble in the denticle's wake altering the flow pressure distribution of the aerofoil to enhance suction and (ii) streamwise vortices that replenish momentum loss in the boundary layer due to skin friction. Our findings not only open new avenues for improved aerodynamic design, but also provide new perspective on the role of the complex and potentially multifunctional morphology of shark denticles for increased swimming efficiency.

1. Introduction

Systems that move suspended within a fluid, such as airplanes, wind turbines, drones and helicopters, all benefit from increased lift-to-drag ratios which results in lower energy consumption [1]. Motivated by this need, two main strategies have been proposed to maximize the lift and minimize the drag. On one hand, several active flow control methods, which involve the addition of auxiliary power into the system, have been demonstrated for both drag reduction and lift augmentation [2–6]. On the other hand, it has also been shown that passive flow control strategies based on geometric modifications are capable of altering lift and drag [7–17]. These include vortex generators [7–13], Gurney flaps [13–15] and winglets [16,17], which reduce drag and increase lift by passively altering the flow to favourably affect the pressure gradients along the aerofoil. Although active methods typically yield better results than the passive ones, they require the supply of external energy, and in fully automated systems rely on complex sensor technology and algorithm development. By contrast, passive techniques are easy to implement and free from any kind of external energy requirements.

Nature, through the course of evolution, has arrived at structures and materials whose traits often offer inspiration for the design of synthetic systems with unique properties [18–20]. Specifically, biological systems have evolved a wide range of drag reducing mechanisms that have inspired the design of synthetic surfaces [18–27]. Shark skin is one such example and is covered with rigid bony denticles (or scales) that exhibit a plate-like upper section

© 2018 The Author(s) Published by the Royal Society. All rights reserved.

Downloaded from http://rsif.royalsocietypublishing.org/ on February 7, 2018

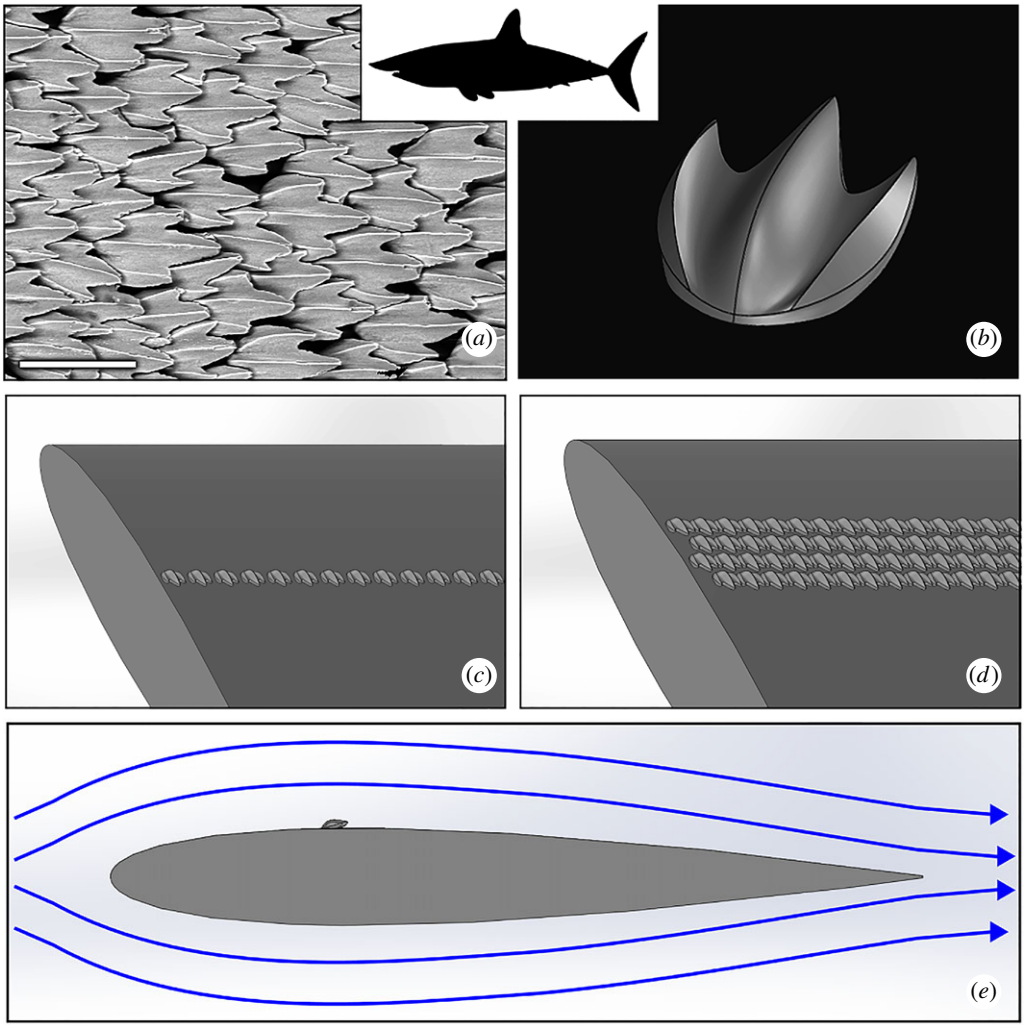

Figure 1. Inspiration, design and testing of shark denticle-inspired vortex generators. (*a*) Environmental scanning electron microscope (ESEM) image of denticles from the shortfin mako shark (scale bar: 200 µm) used in this study and (*b*) its corresponding parametric 3D model. (*c*,*d*) These denticles were arranged in a wide range of different configurations on the suction side of a NACA0012 aerofoil, two examples of which are shown here. (*e*) All of the aerofoils were then tested in fluid flow to evaluate the effect of the denticles on lift and drag.

with ridges, which narrows to a thin neck that anchors into the skin (figure 1*a*,*b*). These intricate structures have inspired the development of several drag reducing surfaces [25], ranging from highly simplified ridge-like geometries [26,27] to complex three-dimensional (3D) printed models that replicate the structural complexities of individual denticles [21–23]. These denticle-inspired surfaces have resulted in a drag reduction of 10% compared to corresponding smooth control surfaces [21–25].

Here, we focus on aerofoils and study experimentally how 3D models of shark denticles arranged on their suction side can passively alter fluid flow. While previous studies have mostly only focused on the effect of shark denticles on drag reduction [21–27], here we demonstrate that the denticles can simultaneously enhance lift and reduce drag, resulting in large lift-to-drag ratios. We study the mechanisms leading to this behaviour and find that shark denticles generate both a recirculation zone (in the form of a short separation bubble in the wake of the denticle) that alters the pressure distribution of the aerofoil to enhance suction, as well as streamwise vortices that reduce drag by replenishing momentum to the flow which would otherwise be lost to skin friction. Guided by these observations, we developed a continuous streamlined geometric perturbation that uses these two mechanisms in a way that further enhances the lift-to-drag ratio.

2. Methods

2.1. Design of aerofoils with shark denticles

In this study, we focused on a smooth aerofoil, arrayed representative models of shark denticles on its suction side (upper surface), and investigated their effect on the aerodynamic performance of the system (figure 1). More specifically, we considered a symmetric NACA0012 aerofoil with aspect ratio $W/L = 2.8$ ($L = 68$ mm being the chord length and W denoting the span length—see electronic supplementary material, section S1 for more details). We arranged on its suction side 3D representative models of a shark denticle based on micro-computed tomography (micro-CT) scans of denticles from *Isurus oxyrinchus* [23]. In figure 2, we show different views of the representative denticle model and indicate the key geometric parameters that define its shape: the chordwise length of the middle ridge (l_c), the chordwise length of the side ridges (l_r), the spanwise length between the outside ridges (l_s), the height of the middle ridge (h_1), the height of the side ridges (h_2) and the tilt angle (θ). In order to explore the parameter space as much as physically possible and to converge on a best design, we created 20 aerofoils characterized by different arrangements (including either single or multiple rows of denticles), sizes and tilt angles of these denticles (see electronic supplementary material, section S1 for more details). Based on measurements of the shark denticles, in our study, we kept $l_c/l_s = 1.37$, $l_c/l_r = 1.25$, $h_1/h_2 = 1.40$ and $l_c/h_1 = 2.95$ constant for all foils. All aerofoils were fabricated

Downloaded from http://rsif.royalsocietypublishing.org/ on February 7, 2018

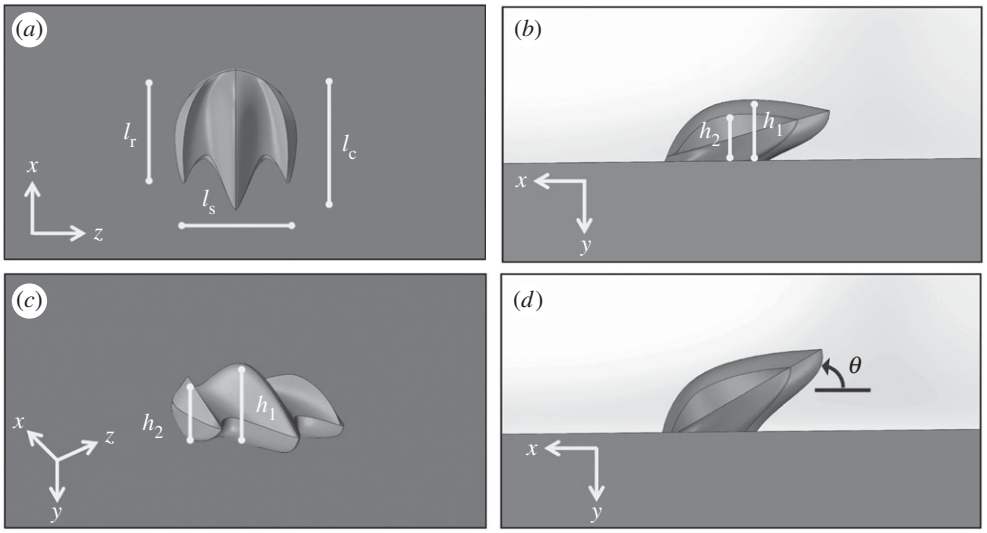

Figure 2. Representative model of the shark denticle. (*a*) Top, (*b*) side and (*c*) isometric view of the representative model of the shark denticle used in this study, along with the corresponding geometric parameters. (*d*) A tilt angle of 15° was used for all foils except one.

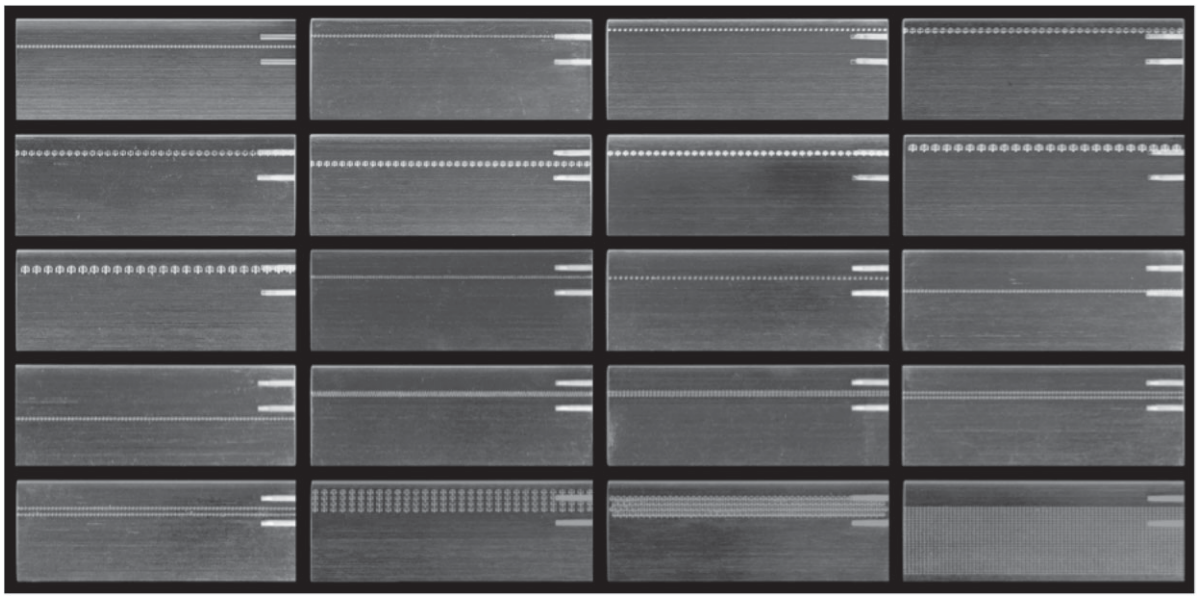

Figure 3. Image of all 20 shark denticle foils tested. The two holes on the upper right of each foil were used to attach the foil to the testing apparatus. A number of different denticle sizes, rows and row positions were tested (see electronic supplementary material, section S1 for more details).

from a transparent photopolymer (RGD81—Stratasys Ltd, Eden Prairie, MN, USA) using an Objet Connex500 3D printer (see figure 3 for images of all 3D printed foils). More details on the diversity of aerofoil designs tested can be found in electronic supplementary material, section S1.

2.2. Experimental testing

Given the relevant Reynolds number ranges for aerodynamic applications (less than 10 000 to greater than 1 000 000) and the dimensional limitations of the 3D printer used to fabricate our test models, these requirements necessitated the use of a water tank for measuring the performance metrics of our aerofoils. Each foil's performance was tested in steady state within a water flow tank (kinematic viscosity $\upsilon = 1 \times 10^{-6}\,\mathrm{m^2\,s^{-1}}$) in the laminar regime with a flow speed of $U = 0.58\,\mathrm{m\,s^{-1}}$, which corresponds to a chord Reynolds number of $Re_c = UL/\upsilon \approx 4 \times 10^4$ [21–23]. The foils were tested at angles of attack, α, from 0° to 24° (post-stall and within the limits of the experimental set-up) in increments of $\Delta\alpha = 2°$. At each angle, the force experienced by the foils parallel to the flow, F_D, and perpendicular to the flow, F_L, were recorded. From these measurements, the dimensionless coefficients of lift (C_L) and drag (C_D) were calculated as

$$C_L = \frac{2F_L}{\rho A U^2}, \quad C_D = \frac{2F_D}{\rho A U^2}, \tag{2.1}$$

where $A = W \times L = 12\,920\,\mathrm{mm^2}$ is the aerofoil planform area (regardless of foil orientation) and $\rho \approx 1000\,\mathrm{kg\,m^{-3}}$ is the density of water. As at the moderate Reynolds number considered in this study, the force measurements can be quite sensitive to the different parameters of the experiment [28], at least six trials were conducted for each of the 20 foils and each presented data point is the average of many tests (with standard error reported). For some foils discussed in this main text, particle image velocimetry (PIV) was also conducted using this water tank. In order to perform the PIV measurements, 10 g of neutrally buoyant, silver-covered glass particles were added to the water tank, and a 10 W continuous-wave argon-ion laser (Innova 300, Coherent Laser Group, CA, USA) was focused at the mid-point of the foil. With this 1–2 mm thick laser sheet shining on the centre of the foil, high-speed videos at 2000 Hz and at a resolution of 1024 pixels by 1024 pixels were taken using a Photron mini-UX100 high-speed video camera. The

Downloaded from http://rsif.royalsocietypublishing.org/ on February 7, 2018

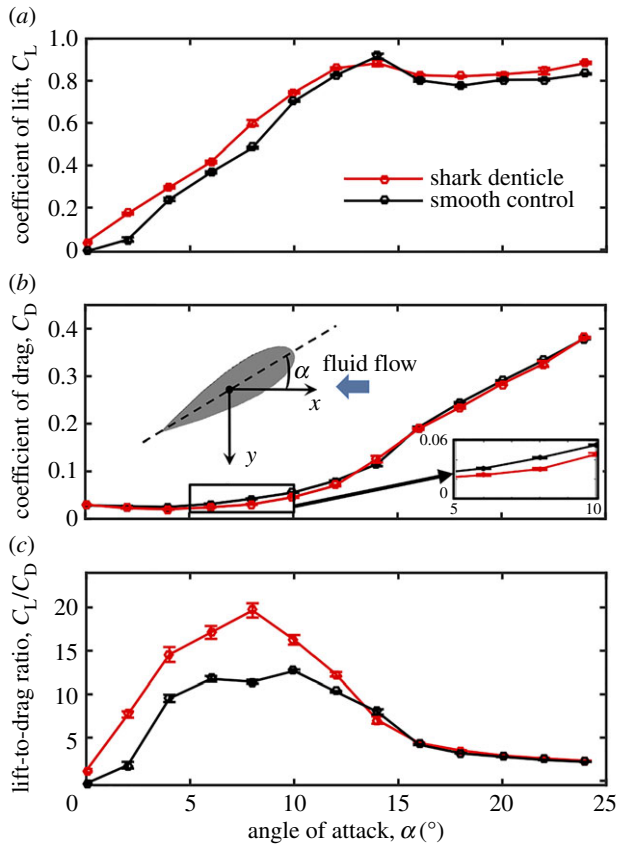

Figure 4. Experimental results for the best shark denticle aerofoil. Evolution of (*a*) lift coefficient, (*b*) drag coefficient and (*c*) lift-to-drag ratio as a function of the angle of attack. In all plots, the results for the best shark denticle foil (red lines) are compared to those for the corresponding smooth control (black lines). Each data point is based on nine total tests and standard error bars are included (note that most error bars are small enough to be contained within the data marker). The inset in (*b*) is a schematic depicting the angle of attack (α) of the aerofoil (-*x* being the direction of fluid flow and -*y* being the direction of lift).

videos were then finally post-processed using LaVision's DaVis software (v. 7.3.1) to obtain the streamlines. See the electronic supplementary material, section S2, for more details on the experimental methods.

3. Results and discussion

As previously shown in many studies focused on vortex generators [8,11,12,29], we find that both the geometry of the denticles and their arrangement have a profound effect on the aerodynamic response of the aerofoils (electronic supplementary material, figures S9–S26). While most foils behaved roughly similar to the denticle-free control, a few of them exhibited significantly enhanced performance (see the electronic supplementary material, section S3, for details). In figure 4, we report results of the experiments for the best performing foil, which comprises a single row of denticles (each of which covers a footprint of roughly 2 mm by 2 mm and has a middle-ridge height of 0.7 mm) placed at 26% along the chord and with a spanwise separation of 1 mm (figure 1*c*). Note that the 26% chordwise placement is consistent with previous work on NACA0012 aerofoils, which has shown that the minimum pressure happens right after this location, making the flow susceptible to separation [29].

The results shown in figure 4 for the best shark denticle foil exhibit three key features. First, we observe an increase in lift at almost all angles of attack for the foil with shark denticles compared to the corresponding smooth control (i.e. $C_L^{shark}/C_L^{control} = 3.55$, 1.24, 1.13, 1.24, 1.06, 1.04, 0.96, 1.03, 1.06 at $\alpha = 2°$, 4°, 6°, 8°, 10°, 12°, 14°, 16°, 18°, respectively—see figure 4*a*). We even find that positive lift is generated at zero angle of attack for the shark denticle foil ($C_L^{shark} = 0.04$ at $\alpha = 0°$), whereas, as expected, we see no lift being generated by the smooth, symmetric control foil for $\alpha = 0°$. Second, the aerofoil with shark denticles reduces drag compared to the smooth control at almost all angles of attack smaller than the angle at which stall occurs ($C_D^{shark}/C_D^{control} = 1.06$, 0.84, 0.81, 0.78, 0.72, 0.83, 0.87 at $\alpha = 0°$, 2°, 4°, 6°, 8°, 10°, 12°, respectively—see figure 4*b*) with drag reduction comparable to previously designed synthetic shark skin surfaces [21–25]. Third, as shown in figure 4*c*, because of the two combined effects described above, we observe substantial enhancements in the lift-to-drag ratio ($C_{L/D} = C_L/C_D$). More specifically, we find that $C_{L/D}^{shark}/C_{L/D}^{control} = 4.23$, 1.53, 1.46, 1.72, 1.28 and 1.19 at $\alpha = 2°$, 4°, 6°, 8°, 10° and 12°, respectively. Such increases are comparable to those observed for the best-reported vane-type low-profile vortex generators for $\alpha \geq 4°$ [8,11,12]. However, the shark denticle morphology outperforms the more traditional designs at low angles of attack ($\alpha < 4°$) (see the electronic supplementary material, section S5, for more details), a condition that is often experienced in use by many systems, including drones, turbines, automobiles and airplanes.

The experimental results shown in figure 4 indicate that there are two driving forces behind the improved lift-to-drag ratio found for the best denticle-containing foil: (i) the enhanced lift, and (ii) the drag reduction at angles of attack prior to stall (i.e. $2° < \alpha < 12°$). By looking at the response of all 20 foils tested (see the electronic supplementary material, figures S9–S26), we find that all of them except two (foils 8 and 20) display lift enhancement at low angles of attack (with aerofoils 11, 14 and 16 showing only very small improvements). These results suggest that such benefit is rather robust, only marginally affected by the location, size and quantity of the geometric perturbations added to the aerofoils. By contrast, we find that the lift improvements at high angles of attack prior to stall, as well as the drag reduction, are sensitive to the location, size and quantity of the denticles (see the electronic supplementary material, section S3, for more details).

To further understand the effect of the denticles on the aerodynamic performance of the aerofoils, first we focused on the robust lift enhancement at low angles of attack. Guided by a previous numerical study that demonstrated that a simple 2D bump arranged on a flat plane can generate a negative pressure coefficient [30], we constructed a foil in which the row of denticles was replaced with a simple 2D bump profile (with non-zero curvature only in the chordwise direction). This bump was arranged in the same chordwise location and had height and leading edge curvature that match those of the shark denticles (see figure 5 for details on the morphology of this aerofoil as well as the electronic supplementary material, section S1). Furthermore, the bump had a streamlined design on its downstream side to reduce its generated pressure drag.

The experimental lift, drag and lift-to-drag ratio for this 2D bump profile on a foil are presented in figure 6 (corresponding numerical results for all of these values are reported in the electronic supplementary material, section S6). If we look specifically at the lift coefficient reported in figure 6*a*, we see that this simple 2D bump profile enhances lift at low angles of attack ($C_L^{2Dbump}/C_L^{control} = 3.08$ and 1.17 at $\alpha = 2°$

Downloaded from http://rsif.royalsocietypublishing.org/ on February 7, 2018

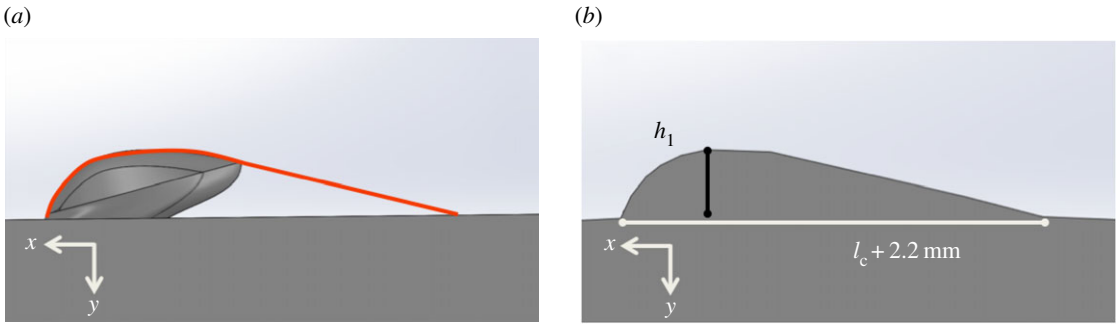

Figure 5. Two-dimensional bump profile. (*a*) Comparison between the profile of the 2D bump (red line) and the representative model of the shark denticle. (*b*) Side view of the 2D bump profile.

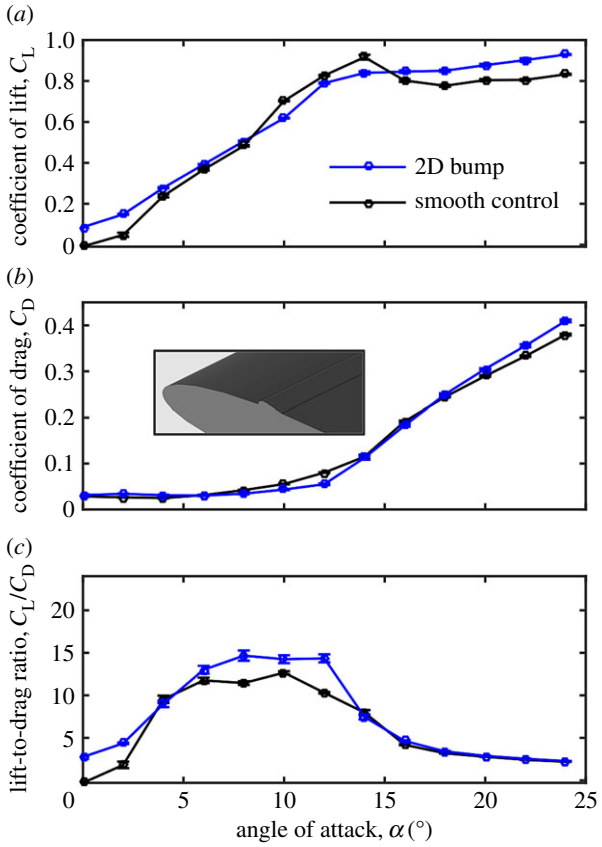

Figure 6. Experimental results for the 2D bump profile on an aerofoil. Evolution of (*a*) lift coefficient, (*b*) drag coefficient and (*c*) lift-to-drag ratio as a function of the angle of attack. In all of the plots, the results for the 2D bump profile on an aerofoil (blue lines) are compared to those for the corresponding smooth control (black lines). Each data point is based on nine total tests and standard error bars are included (note that most error bars are small enough to be contained within the data marker). The inset in (*b*) depicts the morphology of the 2D bump profile.

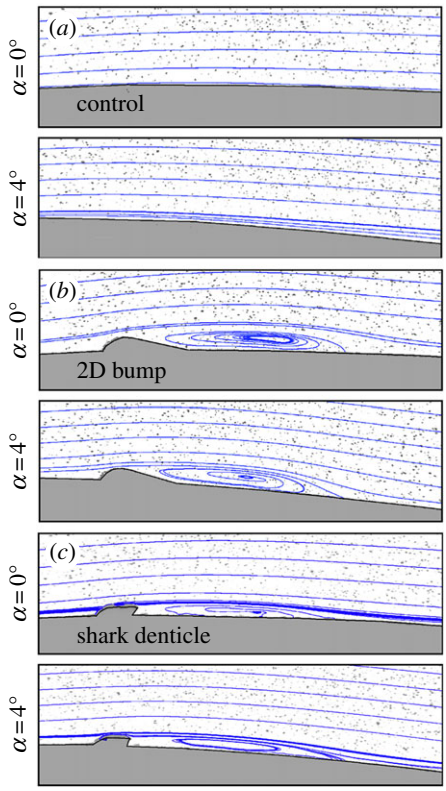

Figure 7. Flow streamlines obtained via particle image velocimetry (PIV). PIV streamlines for the (*a*) smooth, (*b*) 2D bump profile and (*c*) shark denticle foils are shown at $\alpha = 0°$ and 4°, angles at which lift is being significantly enhanced by the 2D bump profile and shark denticle foils. A short separation bubble develops behind both the shark denticle and 2D bump foils, helping to provide further suction and therefore lift for these foils compared to the control.

and $\alpha = 4°$, respectively) and generates non-zero lift at $\alpha = 0°$ ($C_L^{2Dbump} = 0.09$ at $\alpha = 0°$). Interestingly, while at $\alpha = 2°$ and $\alpha = 4°$, the foil with the 2D bump profile generates close to the same amount of lift as the one with the shark denticles ($C_L^{2Dbump}/C_L^{shark} = 0.87$ and 0.94 at $\alpha = 2°$ and 4°, respectively), it results in over twice the amount of lift at zero angle of attack ($C_L^{2Dbump}/C_L^{shark} = 2.41$ at $\alpha = 0°$). These results confirm that the complex shape of the shark denticles arranged on the foil is not necessarily crucial to achieve lift enhancement at low angles of attack, and suggests that a continuous chordwise curved profile can further enhance C_L. However, the results reported in figure 6*a* also demonstrate that the foil with the simple 2D bump profile loses its lift benefits relative to the control at higher angles of attack unlike the shark denticle foil ($C_L^{2Dbumb}/C_L^{control} = 0.88$, 0.95, 0.91 at $\alpha = 10°$, 12°, 14°, respectively). At these angles right before and at stall, it is actually producing less lift than the control. Moreover, we also note that the 2D bump profile does not alter the drag greatly compared to the smooth control (except at $\alpha = 10°$ and 12°—see figure 6*b*). Because of the last two effects, and when compared with the best denticle-containing foil, we find that the 2D bump profile exhibits a significantly lower lift-to-drag ratio across nearly all measured angles of attack (figure 6*c*).

The reason behind the lift benefit at low angles of attack seen by both the shark denticle and 2D bump profile in comparison to the control can be further understood by inspecting the flow streamlines obtained via PIV (see the electronic supplementary material, section S2, for more information on the PIV set-up). The streamlines at $\alpha = 0°$ and 4° shown in figure 7 reveal that, in the presence of

Downloaded from http://rsif.royalsocietypublishing.org/ on February 7, 2018

both the shark denticles and the 2D bump profile, a short separation bubble forms behind their trailing edge. While typically separation bubbles are thought to negatively affect the performance of an aerofoil [8,10], it has also been shown that short separation bubbles (that fully reattach to the aerofoil) can help to maintain a higher level of suction a bit further down the chord of the aerofoil, providing a region over which the pressure distribution along the chord plateaus rather than dropping off further [31]. As such, the short separation bubbles observed in our experiments likely provide additional suction that helps enhance lift.

Having understood how the 2D bump profile and the shark denticles influence lift at low angles of attack, we then turned our attention to lift enhancement at higher angles of attack and drag reduction. The lack of drag reduction seen throughout the majority of angles of attack and loss of lift enhancement at $\alpha > 4^\circ$ for the 2D bump foil suggests strongly that the spanwise curvature of the denticles may play an important role. More specifically, guided by previous studies that showed that geometric perturbations capable of producing streamwise vortices could reduce drag (and prevent losses of lift at higher angles of attack near stall) [8,10–12], we hypothesized that the spanwise curvature of the shark denticles results in the formation of streamwise vortices. In order to confirm this hypothesis, and since the visualization of such vortices via PIV proved challenging due to both the small-scale spatial resolution required and the orientation of the denticles' grooves, we performed computational fluid dynamics (CFD) analyses. The simulations were carried out with ANSYS® CFX, using a combination of a finite-volume and finite-element approach to discretize the Navier–Stokes equations, which were solved by an unsteady fully implicit, fully coupled multigrid solver with the shear stress transport turbulence model (see CFD analysis in the electronic supplementary material, Section S6, for more details) [32]. The numerical results reported in figure 8 for an individual shark denticle on a flat plate not only confirm that the shark denticle morphology creates a short separation bubble in its wake (figure 8*a*) as shown previously via PIV, but also confirm that the shark denticle acts as a vortex generator, as shown clearly by the streamwise vortices forming in the wake of the denticle (figure 8*b*).

These streamwise vortices are likely responsible for drag reduction and also likely help to maintain lift at higher angles of attack by bringing higher momentum fluid from the outer part of the boundary closer to the wall and thus help replenish the momentum in the boundary layer which would have been lost to skin friction. It is further known that the interaction among these vortices is crucial in determining their aerodynamic advantages [33,34]. For instance, placing the vortex generators too close to each other in the spanwise direction can lead to destructive interference of the streamwise vortices, which ultimately reduces the performance of the aerofoil [33,34]. This observation helps explain the high sensitivity of the drag coefficient to the morphology and placement of the denticles that we found in our experiments.

Guided by all these results, we then tried to improve the aerodynamic performance of the aerofoil by designing a geometric perturbation that takes advantage of the multiple mechanisms that were seen to be beneficial in the foils with the shark denticles and the 2D bump. More specifically, we designed a geometric perturbation that combines the ridges

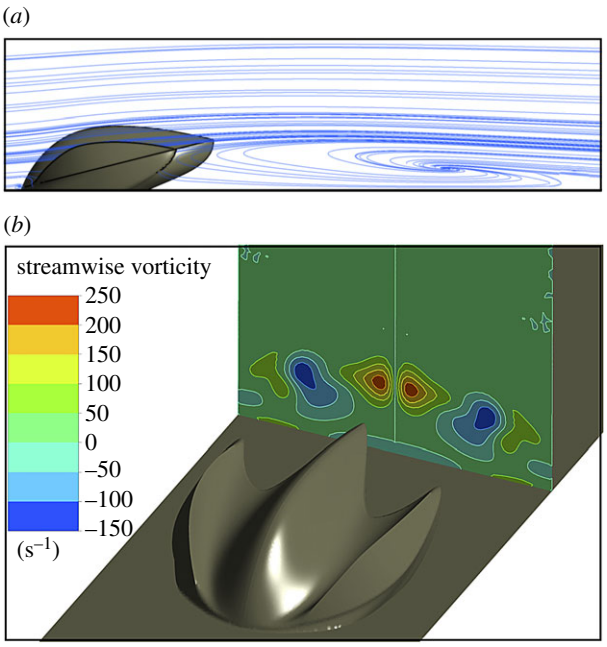

Figure 8. CFD analyses of a shark denticle model on a flat plate. (*a*) Numerical snapshot showing the flow streamlines. Our analyses predict the formation of a short separation bubble in the wake of the denticle. (*b*) Contours of the streamwise vorticity (the rate at which the streamwise-moving fluid is rotating just after the denticle) on a plane perpendicular to the flow just downstream from the denticle. The separation bubble and streamwise vortices shown in (*a*) and (*b*) help to enhance lift and reduce drag when the shark denticle is correctly placed on an aerofoil (see electronic supplementary material, section S3 for more details).

of the shark denticle with the continuous chordwise curved profile of the 2D bump to achieve the lift-to-drag ratio benefits of the shark denticle, while yet also improving the lift further at very low angles of attack (especially $\alpha = 0^\circ$) in the way seen by the 2D bump profile. While this new morphology's chordwise cross-section is designed similarly to that of the 2D bump, its spanwise curvature and morphology resembles that of the denticle except for the fact that it has a continuous sinusoidal-like nature as opposed to the finite nature of the shark denticles placed side-by-side on an aerofoil (see figure 9 for details on the morphology of this profile as well as the electronic supplementary material, section S1). We refer to this new continuous streamlined morphology as the 'continuous shark-inspired profile'.

In figure 10, we report the experimental results for the aerodynamic response of an aerofoil with this continuous shark-inspired profile placed at 26% along the chord. First, focusing on lift at low angles of attack, we find that this aerofoil generates roughly the same amount of lift as the one with the 2D bump profile, and over twice that of the one with shark denticles at $\alpha = 0^\circ$ ($C_L^{cont.}/C_L^{2Dbump} = 1.03$ and $C_L^{cont.}/C_L^{shark} = 2.47$—see figure 10*a*). We also see that the foil with this continuous shark-inspired profile results in coefficients of lift similar to those seen for the cases of the 2D bump profile and shark denticles at other low angles of attack ($C_L^{cont.}/C_L^{2Dbump} = 1.19$, 1.09 and $C_L^{cont.}/C_L^{shark} = 1.04$, 1.03 at $\alpha = 2^\circ$ and 4°, respectively). Second, our results indicate that this continuous shark-inspired profile does not lose these lift benefits as much at higher angles of attack prior to stall. Third, we find that the continuous shark-inspired profile leads to even more drag reduction than the shark denticles (figure 10*b*). This is

Downloaded from http://rsif.royalsocietypublishing.org/ on February 7, 2018

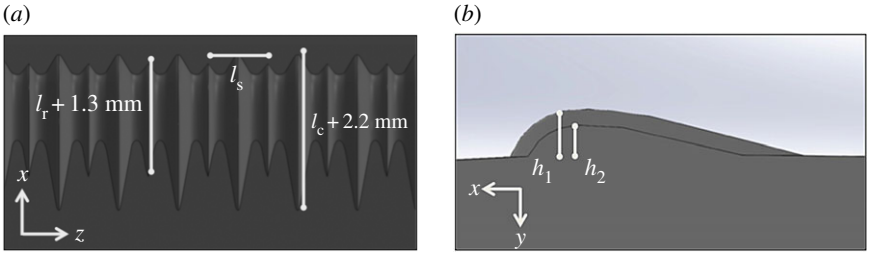

Figure 9. Continuous shark-inspired profile. (*a*) Top and (*b*) side views of the continuous shark-inspired profile.

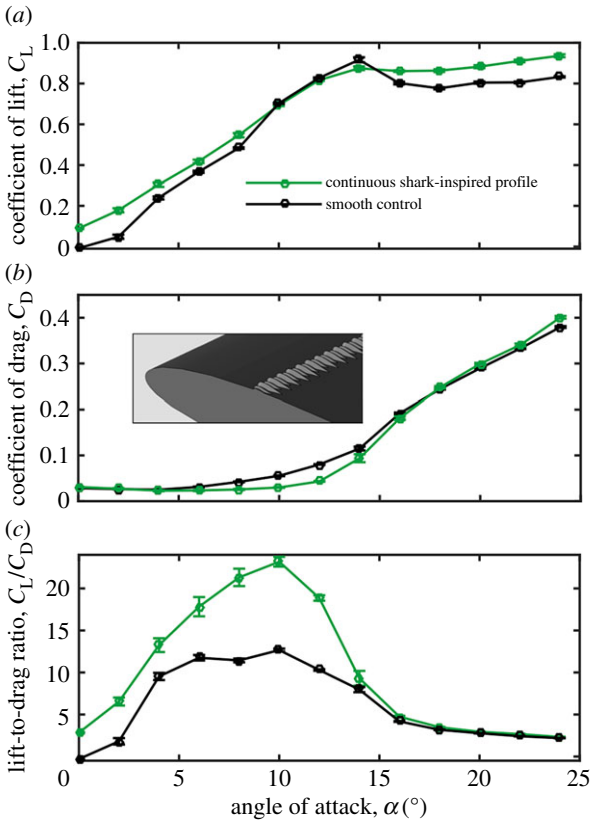

Figure 10. Experimental results for the aerofoil with a continuous shark-inspired profile. Evolution of (*a*) lift coefficient, (*b*) drag coefficient and (*c*) lift-to-drag ratio as a function of the angle of attack. In all plots, the results for the continuous shark-inspired profile (green lines) are compared to those for the corresponding smooth control (black lines). Each data point is based on nine total tests and standard error bars are included (note that most error bars are small enough to be contained within the data marker).

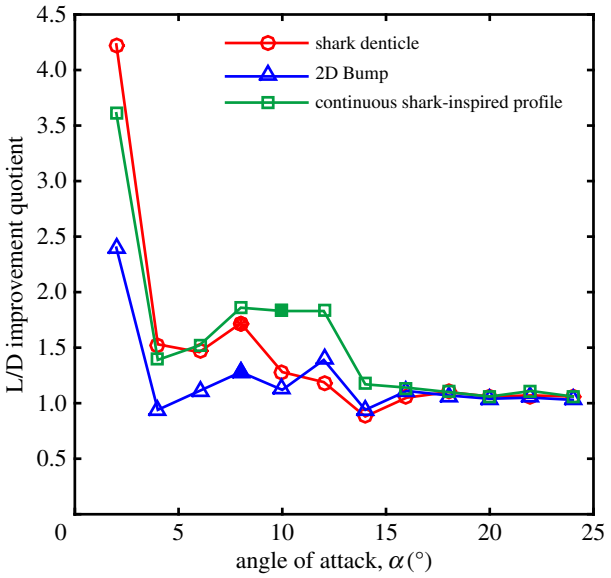

Figure 11. Comparison between the three main foils analysed in this text. The red, blue and green markers correspond to $C_{L/D}^{shark}/C_{L/D}^{control}$, $C_{L/D}^{2Dbump}/C_{L/D}^{control}$ and $C_{L/D}^{cont.}/C_{E/D}^{control}$, respectively. The solid markers represent the angle at which the max L/D for that foil occurs.

especially evident at angles of attack just before stall, with $C_D^{cont.}/C_D^{control} = 0.54$ and 0.53 at $\alpha = 10^\circ$ and 12°, respectively (resulting in $C_D^{cont.}/C_D^{shark} = 0.65$ and 0.62 at $\alpha = 10^\circ$ and 12°, respectively). This may in part be helped by the streamlined nature of the continuous shark-inspired profile. Finally, it is important to note that the observed high lift and low drag lead to large lift-to-drag ratio increases ($C_{L/D}^{cont.}/C_{L/D}^{control} = 3.61$, 1.39, 1.52, 1.86, 1.83 and 1.83 at $\alpha = 2^\circ$, 4°, 6°, 8°, 10° and 12°, respectively—see figure 10*c*).

Specifically, we see from figure 11 (which shows a comparison of the lift-to-drag ratio improvements of all three main foils discussed in this manuscript) that the continuous shark-inspired profile outperforms the 2D bump profile at all angles of attack and the shark denticle at just about all angles of attack (see the electronic supplementary material, section S4, for more details). This is because the continuous shark-inspired profile is able to produce the same lift benefits as the 2D bump at low angles of attack (especially $\alpha = 0^\circ$) without losing these lift benefits as much at higher angles of attack (like the 2D bump does), in addition to greatly reducing drag at higher angles (like the shark denticle is able to). Note that in figure 11 we also indicate with a filled in marker the angle at which the maximum lift-to-drag ratio occurs for each foil. Again, we find that the continuous shark-inspired profile produces the greatest improvement at this angle.

In addition to these great lift-to-drag ratio improvements, this continuous shark-inspired profile has another important advantage over the other foils discussed here. Although there has been increased interest in recent years aimed at reproducing the hydrodynamic performance of shark denticles for use on engineered surfaces, one major obstacle to the mass production of these shark skin-inspired geometries has been the structural complexity of the denticles. While it has been demonstrated previously that it is possible to replicate these forms through the use of 3D printing [23], this approach is unfortunately not scalable, and the undercuts and overhangs present on the native denticles prevent the direct moulding of these specific geometries using conventional manufacturing strategies. The continuous shark-inspired profile described here circumvents these problems and is easily amendable to roll-to-roll embossed fabrication, bringing this technology one step closer to large-scale adoption for aquatic and aerospace applications.

Downloaded from http://rsif.royalsocietypublishing.org/ on February 7, 2018

4. Conclusion

In this study, we have taken inspiration from shark denticles to design a set of profiles that significantly improve the aerodynamics of aerofoils. In contrast to previous studies on shark skin that have mostly focused on drag reduction/thrust improvement [21–27], we showed that the denticles also generate lift, resulting in high lift-to-drag ratio improvements. Specifically, we found comparable results to those of the best previously reported low-profile vortex generators at higher angles of attack near stall, and even much higher improvements at low angles of attack ($\alpha < 4^\circ$) [8,11,12]. The remarkable results shown here were achieved by using two mechanisms. First, the shark-inspired profiles trip the boundary layer and generate a short (reattaching) separation bubble that provides extra suction along the chord and thereby enhances lift. Second, the spanwise curvature of the denticles helps to generate streamwise vortices that can lead to drag reduction and prevent lift losses at higher angles of attack. While in this study we have considered the ideal case of the denticles' ridges perfectly parallel to the flow, future work will investigate how sensitive the aerodynamic response of the aerofoils is to the orientation of the denticles with respect to the flow.

It is important to note that the flow regime considered in this study ($Re_c \approx 4 \times 10^4$) is relevant for many systems, including interior portions of wind turbine blades, helicopter blades, drones and autonomous underwater vehicles. Moreover, some of the mechanisms discovered here can hold also for higher flow regimes and can be used to improve movement through air and water. Finally, the results discussed here may have implications for understanding the function of shark denticle morphology. Shark skin denticles have been shown to alter the position and strength of the leading edge vortex in experimental studies [21], and it is likely that the lift effects observed here contribute to a thrust enhancement effect of shark skin resulting in increased self-propelled swimming speeds [23].

Ethics. No experiments were conducted on humans or live animals.

Data accessibility. All supporting data are either presented in the main text or electronic supplementary material.

Authors' contributions. A.G.D., M.S., K.B. and G.V.L. conceived the study and experiments. A.G.D. and J.C.W. developed and manufactured the aerofoils. A.G.D. and M.S. conducted experiments. All authors contributed to the analysis. All authors contributed to and approved the final manuscript.

Competing interests. We declare we have no competing interests.

Funding. The research was supported by Office of Naval Research grant no. N00014-09-1-0352 to G.V.L., monitored by T. McKenna. K.B. gratefully acknowledges support by the National Science Foundation through grant no. DMREF-1533985.

Acknowledgements. The authors would like to thank Fanli Liu, Shirui Peng, Dylan Wainwright, Li Wen, Alperen Degirmenci and Sijie Tong for their help with the project. The authors would also like to thank Harvard's John A. Paulson School of Engineering and Applied Sciences and the Wyss Institute. Furthermore, the authors would like to thank ANSYS® for providing computational resources. M.S. further acknowledges support from the Educational Foundation of the University of South Carolina.

References

1. Raymer D. 2012 *Aircraft design: a conceptual approach*, 5th edn. New York, NY: AIAA.
2. Amitay M, Smith B, Glezer A. 1998 *Aerodynamic flow control using synthetic jet technology*. In *36th AIAA Aerospace Sciences Meeting and Exhibit, Reno, NV, 12 January*. Reston, VA: AIAA.
3. Kiedaisch J, Nagib H, Demanett B. 2006 *Active flow control applied to high-lift airfoils utilizing simple flaps*. In *3rd AIAA Flow Control Conference, San Francisco, CA, 5 June*. Reston, VA: AIAA.
4. Pack L, Schaeffler N, Yao C, Seifert A. 2002 *Active control of flow separation from the slat shoulder of a supercritical airfoil*. In *1st Flow Control Conf., St Louis, MO, 26 June*. New York, NY: AIAA.
5. Kiedaisch J, Demanett B, Reinhard P, Nagib H. 2007 *Active flow control for high lift airfoils: dynamic flap actuation*. In *45th AIAA Aerospace Sciences Meeting and Exhibit, Reno, NV, 10 January*. Reston, VA: AIAA.
6. Amitay M, Parekh DE, Smith DR, Kibens V, Glezer A. 2001 Aerodynamic flow control over an unconventional airfoil using synthetic jet actuators. *AIAA J.* **39**, 361–370. (doi:10.2514/2.1323)
7. Lin JC, Howard FG, Selby GV. 1990 Small submerged vortex generators for turbulent flow separation control. *J. Spacecr. Rockets* **27**, 503–507. (doi:10.2514/3.26172)
8. Lin JC. 2002 Review of research on low-profile vortex generators to control boundary-layer separation. *Prog. Aerosp. Sci.* **38**, 389–420. (doi:10.1016/S0376-0421(02)00010-6)
9. Yao C, Lin J, Allen B. 2002 *Flowfield measurement of device-induced embedded streamwise vortex on a flat plate*. In *1st Flow Control Conference*. Reston, VA: American Institute of Aeronautics and Astronautics.
10. Kerho M, Hutcherson S, Blackwelder RF, Liebeck RH. 1993 Vortex generators used to control laminar separation bubbles. *J. Aircr.* **30**, 315–319. (doi:10.2514/3.46336)
11. Lin JC, Robinson SK, McGhee RJ, Valarezo WO. 1994 Separation control on high-lift airfoils via micro-vortex generators. *J. Aircr.* **31**, 1317–1323. (doi:10.2514/3.46653)
12. Lin J. 1999 *Control of turbulent boundary-layer separation using micro-vortex generators*. In *30th Fluid Dynamics Conf.* Reston, VA: AIAA.
13. Storms BL, Jang CS. 1994 Lift enhancement of an airfoil using a Gurney flap and vortex generators. *J. Aircr.* **31**, 542–547. (doi:10.2514/3.46528)
14. Myose R, Papadakis M, Heron I. 1998 Gurney flap experiments on airfoils, wings, and reflection plane model. *J. Aircr.* **35**, 206–211. (doi:10.2514/2.2309)
15. Wang JJ, Li YC, Choi K-S. 2008 Gurney flap—lift enhancement, mechanisms and applications. *Prog. Aerosp. Sci.* **44**, 22–47. (doi:10.1016/j.paerosci.2007.10.001)
16. Guerrero JE, Maestro D, Bottaro A. 2012 Biomimetic spiroid winglets for lift and drag control. *Comptes Rendus Mécanique* **340**, 67–80. (doi:10.1016/j.crme.2011.11.007)
17. Whitcomb RT. 1976 *A design approach and selected wind-tunnel results at high subsonic speeds for wing-tip mounted winglets*. Hampton, VA: NASA Langley Research Center.
18. Bar-Cohen Y. 2005 *Biomimetics*, pp 495–513. Boca Raton, FL: CRC Press.
19. Benyus JM. 1997 *Biomimicry. Innovation inspired by nature*. New York, NY: Harper Collins.
20. Patek SN. 2014 Biomimetics and evolution. *Science* **345**, 1448–1449. (doi:10.1126/science.1256617)
21. Oeffner J, Lauder GV. 2012 The hydrodynamic function of shark skin and two biomimetic applications. *J. Exp. Biol.* **215**, 785–795. (doi:10.1242/jeb.063040)
22. Lauder GV, Wainwright DK, Domel AG, Weaver JC, Wen L, Bertoldi K. 2016 Structure, biomimetics, and fluid dynamics of fish skin surfaces. *Phys. Rev. Fluids* **1**, 1044 (doi:10.1103/PhysRevFluids.1.060502)
23. Wen L, Weaver JC, Lauder GV. 2014 Biomimetic shark skin: design, fabrication and hydrodynamic function. *J. Exp. Biol.* **217**, 1656–1666. (doi:10.1242/jeb.097097)
24. Bechert DW, Bruse M, Hage W. 2000 Experiments with three-dimensional riblets as an idealized

Downloaded from http://rsif.royalsocietypublishing.org/ on February 7, 2018

model of shark skin. *Exp. Fluids* **28**, 403–412. (doi:10.1007/s003480050400)

25. Dean B, Bhushan B. 2010 Shark-skin surfaces for fluid-drag reduction in turbulent flow: a review. *Phil. Trans. R. Soc. A* **368**, 4775–4806. (doi:10.1098/rsta.2010.0201)
26. Fu YF, Yuan CQ, Bai XQ. 2017 Marine drag reduction of shark skin inspired riblet surfaces. *Biosurface Biotribol.* **3**, 11–24. (doi:10.1016/j.bsbt.2017.02.001)
27. Sareen A, Deters RW, Henry SP, Selig MS. 2014 Drag reduction using riblet film applied to airfoils for wind turbines. *J. Sol. Energy Eng.* **136**, 021007. (doi:10.1115/1.4024982)
28. Tank J, Smith L, Spedding GR. 2017 On the possibility (or lack thereof) of agreement between experiment and computation of flows over wings at moderate Reynolds number. *Interface Focus* **7**, 20160076. (doi:10.1098/rsfs.2016.0076)
29. Mueller-Vahl H, Pechlivanoglou G, Nayeri CN, Paschereit CO. 2012 Vortex generators for wind turbine blades: a combined wind tunnel and wind turbine parametric study. In *Volume 6: Oil and Gas Applications; Concentrating Solar Power Plants; Steam Turbines; Wind Energy, Copenhagen, Denmark, 11 June*.
30. Baskaran V, Smits AJ, Joubert PN. 1987 A turbulent flow over a curved hill Part 1. Growth of an internal boundary layer. *J. Fluid Mech.* **182**, 47–83. (doi:10.1017/S0022112087002246)
31. Roberts W. 1979 *Calculation of laminar separation bubbles and their effect on airfoil performance*. In *17th Aerospace Sciences Meeting 18, New Orleans, LA, 15 January*, pp. 25–31. Reston, VA: AIAA.
32. ANSYS® Academic Research, Release 14.0, Help System, ANSYS CFX-Solver Theory Guide, ANSYS, Inc.
33. Ashill P, Fulker J, Hackett K. 2002 *Studies of flows induced by Sub Boundary Layer Vortex Generators (SBVGs)*. In *40th AIAA Aerospace Sciences Meeting & Exhibit, Reno, NV, 14 January*. Reston, VA: AIAA.
34. Tai T. 2002 *Effect of micro-vortex generators on V-22 aircraft forward-flight aerodynamics*. In *40th AIAA Aerospace Sciences Meeting & Exhibit, Reno, NV, 14 January*. Reston, VA: AIAA.

Supporting Information for Shark Skin-Inspired Designs That Improve Aerodynamic Performance

August G. Domel, Mehdi Saadat, James C. Weaver, Hossein Haj-Hariri, Katia Bertoldi, George V. Lauder

S1. Geometry

In this section, we provide geometric details on all of the different foils considered in this study. All the airfoils tested in this study are based on a symmetric NACA0012 airfoil with aspect ratio W/L=2.8 (L=68mm being the chord length and W denoting the span length – see Fig. S1). We first characterized the aerodynamic performance of the smooth airfoil, and then investigated how the coefficients of lift and drag are affected when different geometric perturbations are arranged on its suction side.

Models of all foils were created using SolidWorks (SolidWorks Corp., Waltham, MA, USA). These models were exported as stl files and 3D printed using an Objet Connex500 3D printer (Stratasys Ltd, Eden Prairie, MN, USA). The foils were printed from a transparent photopolymer (RGD810) on the Connex500 3D printer. Any supporting material used to print the foil was easily removed using a water jet (1). Because this 3D printer has some precision limitations with which smooth surfaces can be printed, the leading edge of the foils had some slight roughness with a root-mean-square height of roughly 8 microns, measured using surface profilometry (2, 3).

S1.1 Smooth Control

In Fig. S1 we show a model of the airfoil used as the smooth control in this study. It consists of a symmetric NACA0012 airfoil with aspect ratio W/L=2.8 and no perturbation on its faces.

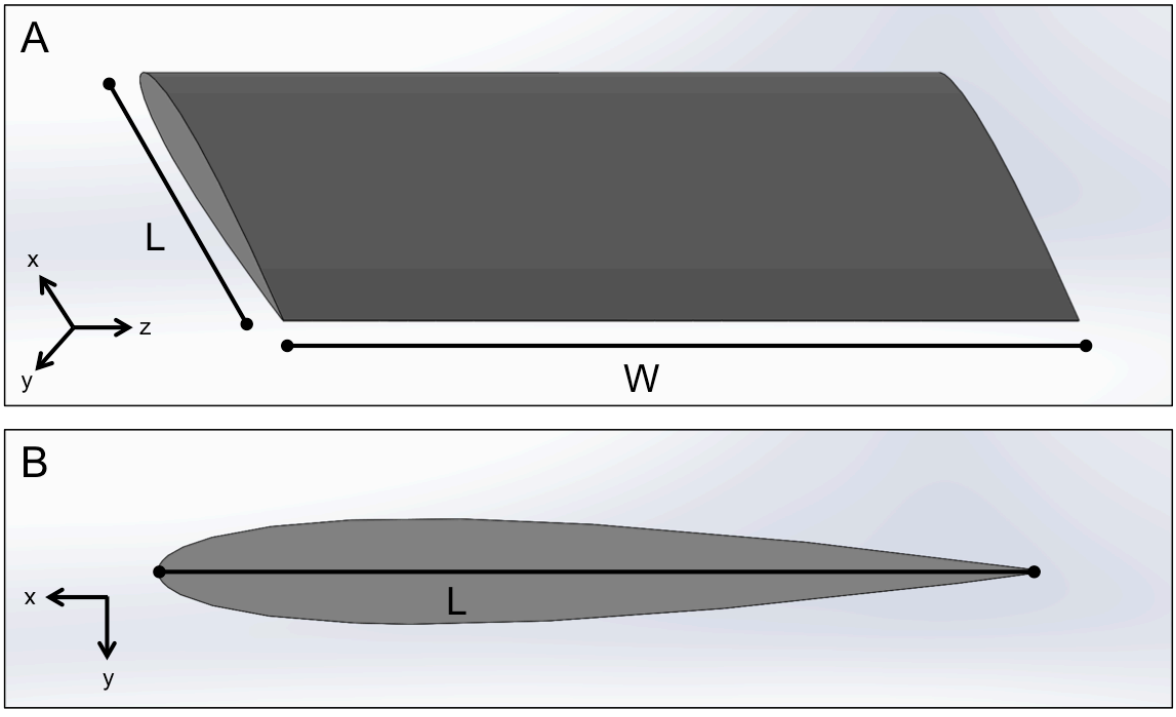

Figure S1: (A) Isometric and (B) cross-sectional views of the smooth NACA0012 airfoil.

S1.2 Airfoils with Shark Denticles

We designed 20 airfoils characterized by different arrangements, sizes, and tilt angles of representative models of shark denticles attached to their suction side (see Fig. S2).

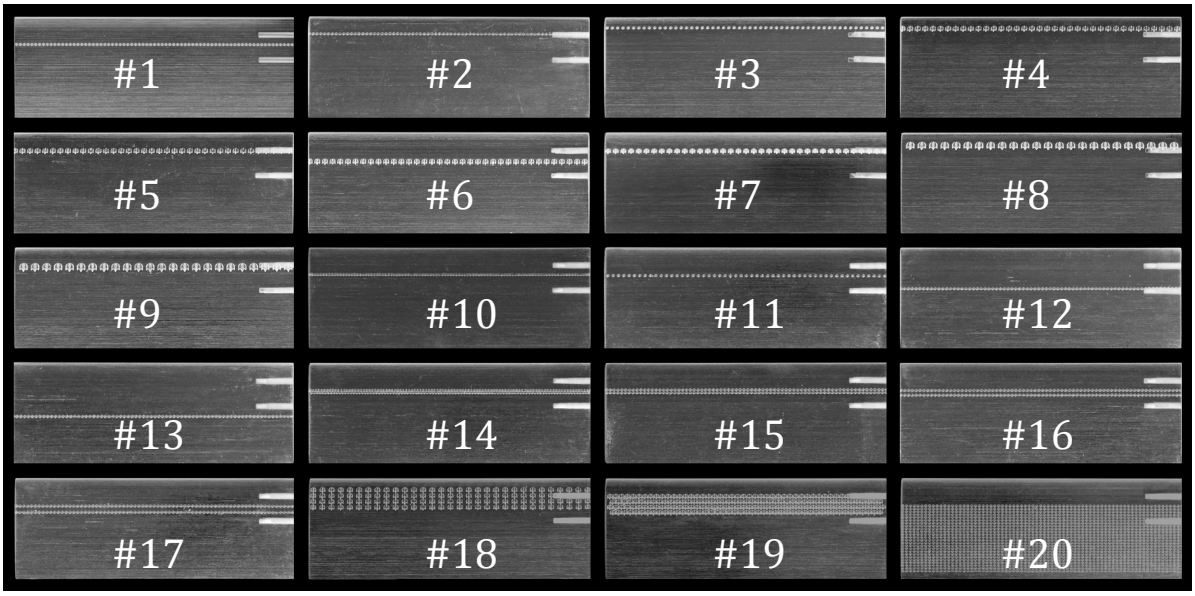

Figure S2: Image of all 20 shark denticle foils tested. The two holes on the upper right of each foil were used to attach the foil to the testing apparatus.

Representative model of shark denticles: The 3D parameterized model of a single representative denticle from a shortfin mako shark (Isurus oxyrinchus) was constructed using a microCT scanner (XradiaVersaXRM-500, at Cornell University, Institute of Biotechnology) and meshed using Mimics 3D (Materialise Inc., Leuven, Belgium). Details of shark denticle modeling are also available in Wen et al. (2014, 2015) (1, 4). A representative model is shown in Fig. S3. There, l_c is the chordwise length of the middle ridge, l_r is the chordwise length of the side ridges, l_s is the spanwise length between the outside ridges (the middle ridge is placed in the middle between these two ridges), h_1 is the height of the middle ridge, and h_2 is the height of the side ridges. Based on measurements of the shark denticles, in our study we kept $l_c/l_s = 1.37$, $l_c/l_r = 1.25$, $h_1/h_2 = 1.40$, and $l_c/h_1 = 2.95$ constant for all foils. Moreover, all denticles (except those arranged on foil #7) were placed with a 15° angle of tilt (θ) (see Fig. S3*D*). An additional 15° of tilt (meaning the denticles were rotated 15° further counterclockwise about their center) was given to the denticles arranged on foil #7. Additional details on the geometry of the denticles arranged on the 20 different foils considered in this study are provided in Table S1.

Denticle arrangement: All denticles were placed on the suction side of the airfoils with their grooves aligned parallel to the chordwise direction (see Fig S2). 13 foils (Foils #1 - #13) comprise a single row of denticles placed at different distances, d/L, along the chord (d denoting the distance from the leading edge to the front of the row of denticles – see Fig S4*A*) and with a spanwise separation b varying between 0 and 3 mm (see Fig. S4*B* and Table S1 for details). The remaining 7 foils (Foils #14 - #20) comprise multiple rows of denticles, arranged either according to a linear (see Fig. S4*C*) or staggered pattern (see Fig. S4*D*). Note that for these foils the geometric parameter d as specified in Table S1 indicates the distance from the leading edge to the front of the first row of denticles. Moreover, in Table S1 "closely packed" refers to denticles spaced as closely as possible without physically touching, as shown in Fig. S4*D*.

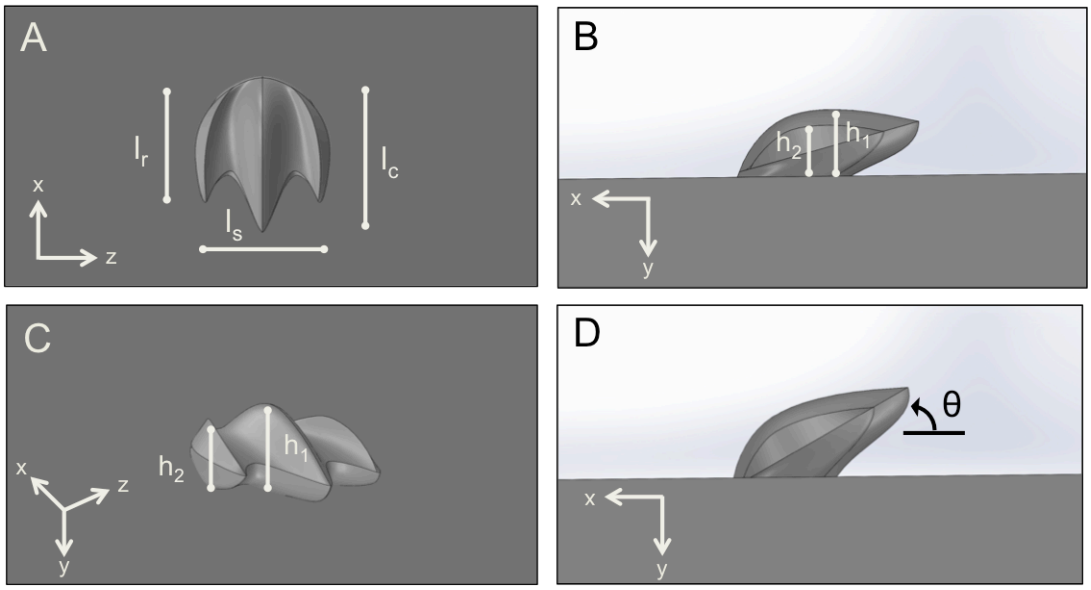

Figure S3: (A) Top, (B) side, and (C) isometric view of the representative model of the shark denticle used in this study, along with the corresponding geometric parameters. (D) A tilt angle θ=15° was used for all denticles except for foil #7, for which θ=30°.

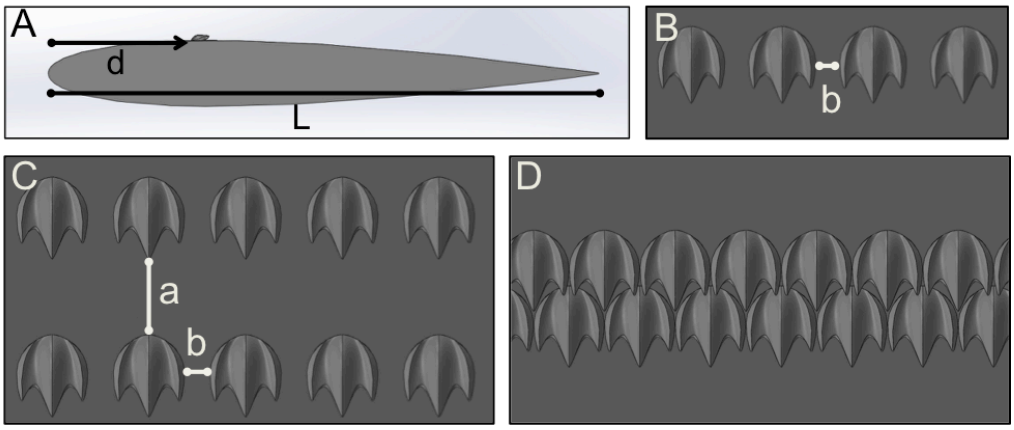

Figure S4: (A) Side view of the foil showing the chordwise placement of the denticles on its suction side. (B) Foils #1 - #13 have a single row of denticles with a spanwise separation *b*. (C)-(D) Foils #14 - #20 comprise multiple rows of denticles arranged either on a (C) linear or a (D) staggered pattern.

Table S1: Geometric parameters characterizing the 20 different shark denticle foils considered in this study. Images of all 20 shark denticle foils are shown in Fig. S2.

Foil #	Pattern	# of Rows	Chordwise Separation, a [mm]	Spanwise Separation, b [mm]	Location along Chord, d/L	Size of Denticle, l_c [mm]	Tilt Angle of Denticle, θ [deg.]
1	linear	1	n/a	1	0.26	2	15
2	linear	1	n/a	1	0.16	2	15
3	linear	1	n/a	2	0.10	2	15
4	linear	1	n/a	2	0.10	4	15
5	linear	1	n/a	2	0.16	4	15
6	linear	1	n/a	2	0.26	4	15
7	linear	1	n/a	2	0.16	4	30
8	linear	1	n/a	3	0.10	6	15
9	linear	1	n/a	3	0.16	6	15
10	linear	1	n/a	0	0.26	2	15
11	linear	1	n/a	2	0.26	2	15
12	linear	1	n/a	1	0.38	2	15
13	linear	1	n/a	1	0.50	2	15
14	staggered	2	closely packed	closely packed	0.26	2	15
15	linear	2	closely packed	1	0.26	2	15
16	linear	2	1	1	0.26	2	15
17	linear	2	2	1	0.26	2	15
18	linear	4	closely packed	3	0.10	4	15
19	staggered	4	closely packed	closely packed	0.16	4	15
20	linear	26	closely packed	1	0.26	2	15

S1.3 Airfoil with 2D Bump Profile

To further understand the effect of the denticles on the aerodynamic performance of the foils, we then considered a foil in which one row of denticles is replaced with a simple 2D bump profile, which has non-zero curvature only in the chordwise direction.

Fig. S5 below shows the morphology of the 2D bump foil. The leading edge curvature matches the shark denticle middle ridge leading edge curvature. However, rather than having an overhang like the shark denticle does, the bump attaches to the foil downstream from where the shark denticle middle ridge ends. This gives the 2D bump a streamlined nature so as to reduce pressure drag. Note that all parameters and dimensions (h_1, l_s, d, L, W) shown in Fig. S5 match exactly that of the best shark denticle foil (Foil #1). Specifically, h_1=0.7mm, l_c=2mm, d/L=0.26, L=68mm and W/L=2.8.

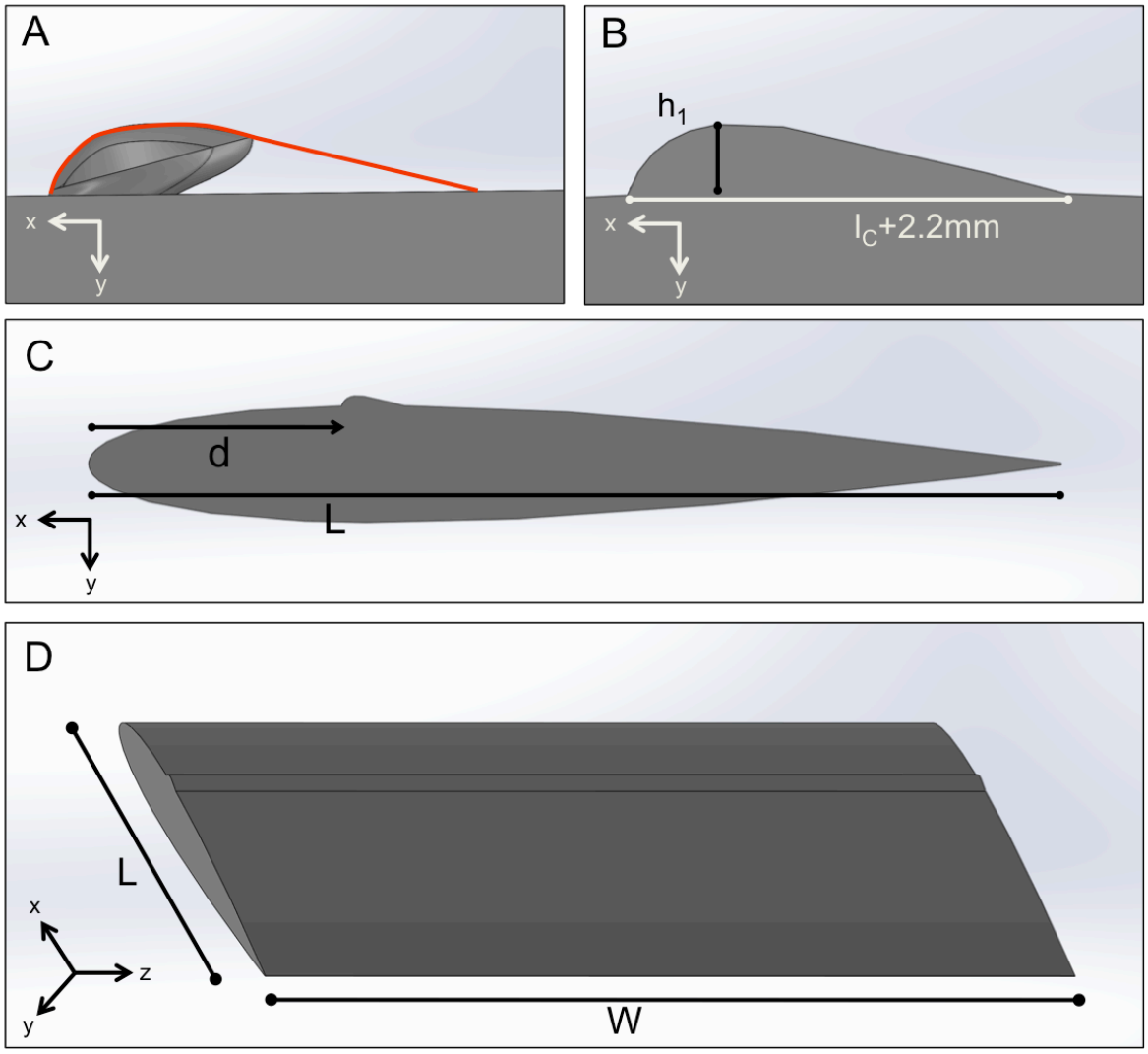

Figure S5: (A) Comparison between the profile of the 2D bump (red line) and the representative model of the shark denticle. (B) Side view of the 2D bump. (C) Chordwise placement of the 2D bump on the foil (d/L=0.26). (D) Isometric view of the 2D bump foil.

S1.4 Airfoil with Continuous Shark-Inspired Profile

Guided by our experiments, we then tried to improve the aerodynamic performance of the airfoil by designing a geometric perturbation that takes advantage of the multiple mechanisms that were seen to be beneficial in airfoils with the shark denticles and the 2D bump profile. More specifically, we designed a geometric perturbation that merges the ridges of the shark denticle with the continuous chordwise curved profile of the 2D bump profile. As such, we refer to this morphology as the continuous shark-inspired profile.

In Fig. S6 we show top, side, and isometric views of the continuous shark-inspired profile. Essentially, this morphology can be thought of as one continuous shark denticle that runs the full span of the foil at a chordwise placement of d/L = 0.26. The leading edge chordwise curvature matches that of the shark denticle (just like the 2D bump profile did). This morphology also has an extremely similar structure as that of the denticle with a long chordwise middle ridge between two smaller side ridges (the side ridges have been extended an extra 1.3mm and the middle ridge an extra 2.2mm so as to give this profile a very streamlined extended shape like that of the 2D bump profile, yet with pronounced chordwise ridges like that of the denticle). Similarly to foil #1, h_1=0.7mm, h_2=0.5mm, l_s=1.5mm, l_c=2mm, l_r=1.6mm, d/L=0.26, L=68mm, W/L=2.8.

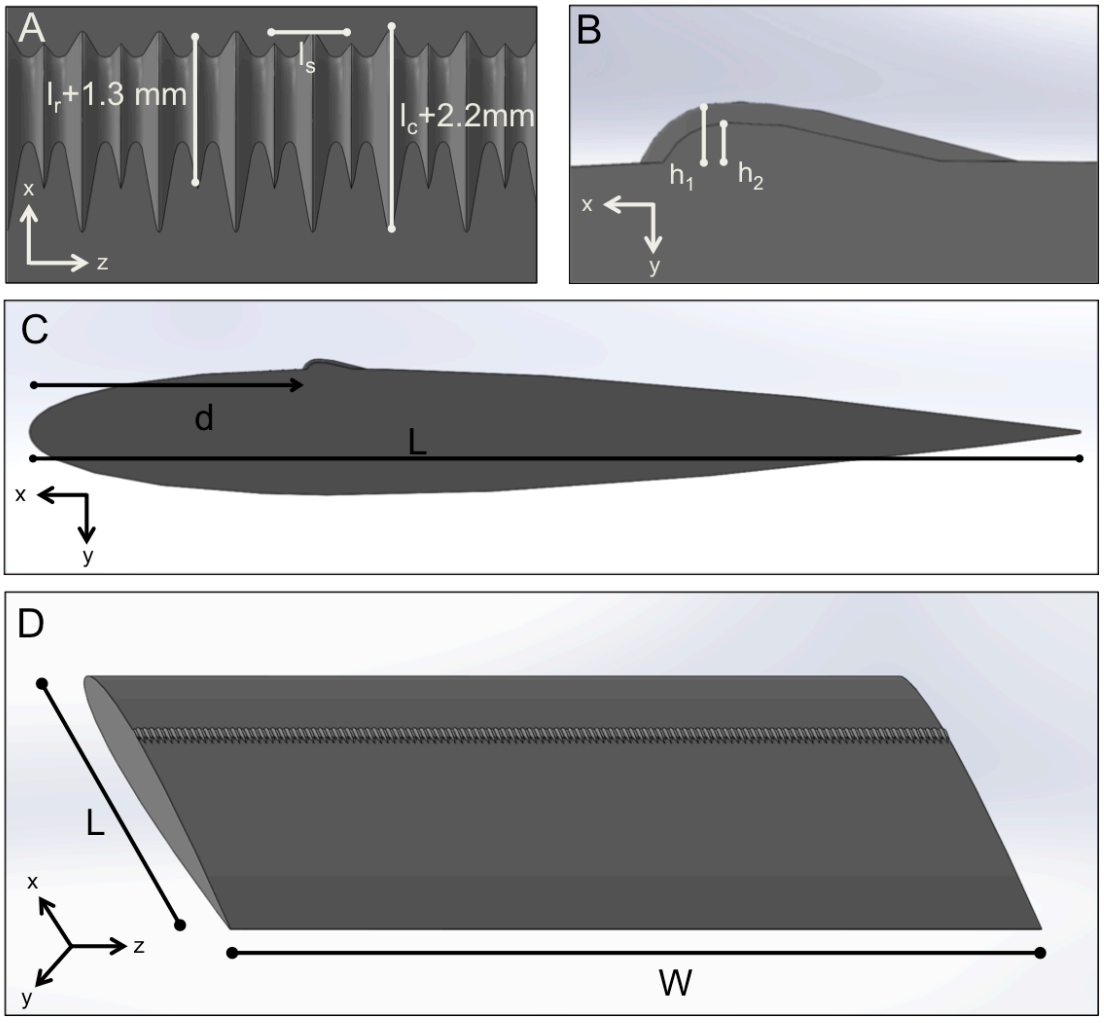

Figure S6: (A) Top and (B) side views of the continuous shark-inspired profile. (C) Chordwise placement of the profile on the foil (d/L=0.26). (D) Isometric view of the continuous shark-inspired foil.

S2. Experimental Setup

Each foil's aerodynamic performance was tested in steady state within the water flow tank shown in Fig. S7 (kinematic viscosity υ=1x10^{-6} m^2/s). All tests were conducted in the laminar regime with a flow speed of U=0.58m/s, which corresponds to a chord Reynolds number of $Re_c=UL/\upsilon\approx$4x10^4. PIV was conducted using this water tank as well. 10g of neutrally-buoyant, sliver-covered glass particles were added to the water tank, and a 10W continuous-wave argon-ion laser (Innova 300, Coherent Laser Group, CA, USA) was focused at the middle of each foil for which PIV was conducted. Using a Photron mini-UX100 high-speed video camera, high speed videos at 2000Hz and at a resolution of 1024 pixels by 1024 pixels were taken. Then, using LaVision's DaVis software (v 7.3.1), the videos were post-processed to obtain the streamlines.

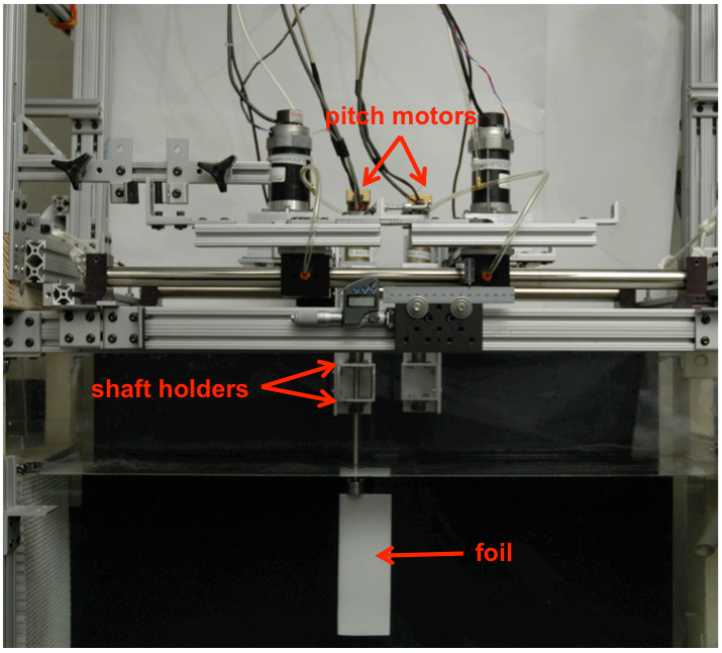

Figure S7: Experimental flow tank setup used to test the foils. The pitch motors are used to determine the angle of attack of the foil. The shaft holders support the foil within the tank. The tanks working section dimensions are 26cm x 26cm x 80cm.

It is important to note that, at the moderate Reynolds numbers considered in this study, the response of the foils is strongly influenced by the unavoidable small imperfections introduced both during fabrication and testing (8). Therefore, the following points need to be considered when comparing the results reported in this study with available foil data in the literature.

1. **Surface roughness of the airfoil.** Surface roughness of an airfoil can certainly influence flow separation and measured C_L and C_D values, and no manufactured airfoil is completely smooth. We measured the surface roughness of our 3D printed foils using quantitative surface profilometry and report a root-mean-square surface feature height of 8 microns (2, 3).

2. **Turbulence intensity.** Turbulence intensity in the tank can also influence patterns of the fluid flow over a foil. The turbulence intensity values measured for our experimental setup are roughly 3-5%.

3. **Drag on the holding rod.** We measured forces on the holding rod in the absence of the foil over a range of angles of attack (since rotating the holding rod could potentially affect measured drag). Mean values of rod drag and lift were subtracted at each point for the data reported in this study.

4. **Tip effects and surface waves.** The upper and lower edges of the tested foils were roughly 3cm from the tank bottom and free water surface. Some interaction of flow over the foil and these surfaces is inevitable, but we were not able to detect any effects of foil surface interactions that affected our experimental data.

5. **Trailing edge thickness.** 3D printed airfoils are subject to the challenges of 3D printing resolution in general, and a perfectly sharp tailing edge is particularly difficult to achieve. Our foils were printed at high resolution on an Objet Connex 500 printer which has state-of-the art resolution capability, but the trailing foil edge is likely not as sharp as might occur in manufactured and polished aluminum airfoils.

6. **Asymmetry in manufactured airfoils.** Even though there are necessarily some minor asymmetries due to additive printing, we made every effort to ensure that our 3D printed airfoils were symmetrical and met NACA0012 profile standards.

7. **Calibration and airfoil alignment.** Airfoil calibration and alignment is one of the most critical and yet challenging issues in conducting static tests on airfoils (8). We expended considerable effort to ensure that our calibration was accurate and that airfoil alignment provided accurate, symmetric results for the smooth control foil. Symmetrical data were obtained when the control foil was moved in both directions (i.e., measurements of lift and drag forces showed similar patterns when the foil was rotated both clockwise and counterclockwise). In order to be able to obtain these accurate, symmetric results, the data had to be calibrated from the raw forces read by the transducer. Because it is very difficult to perfectly align the transducer with the foil, some β angle must be introduced to calibrate, calculate, and ensure symmetric and accurate results in the smooth control foil. Specifically, since the force transducer is locked in with the foil during experiments, it rotates with the foil as the foil is rotated to test the different angles of attack. If we denote with F_x and F_y the forces along the x- and y-direction read by the transducer (see Fig. S8), it follows that the lift and drag force on the foil can be calculated as

$$\boldsymbol{F_D = F_x * cos(\alpha + \beta) + F_y * sin(\alpha + \beta)} \quad \text{(S1)}$$

$$\boldsymbol{F_L = F_y * cos(\alpha + \beta) - F_x * sin(\alpha + \beta)} \quad \text{(S2)}$$

where α is the angle of attack of the foil and β is the calibration angle to ensure symmetrical results for the foils (see Fig. S8).

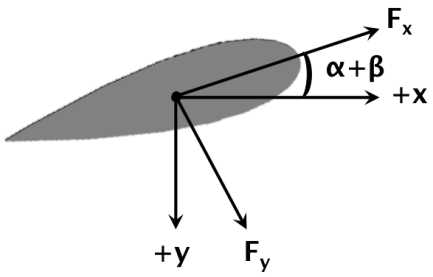

Figure S8: Schematic for calibration.

In addition, we note that the C_L and C_D values of our smooth control at zero angle of attack align well with the literature (8). Differently, a wide range of values of lift and drag has been reported in literature for angles of attack past zero (8). This is undoubtedly due to a rather considerable variation of the parameters (i.e. 7 points described above) among the different investigators.

S3. Experimental Results for All Shark Denticle Foils

In this section, we present the experimentally measured C_L, C_D, and C_L/C_D curves for the considered 20 different shark denticle foils, grouped by the different parameters that were varied. In all plots each data point is based on at least six total tests, and standard error bars are included (error bars are sometimes small enough to be contained within the plotted symbol).

Although in the main text we discuss in detail the response of the best performing shark denticle foil (Foil #1 in Table S1), these experimental data show that there are several other foils that also perform pretty well.

S3.1 Varying Chordwise Position and Size of Denticles

In this section, we consider airfoils with denticles of different sizes and at different chordwise positions (Foils #1-6, #8-9 as shown in Fig. S9). Data for each of these foils can be found in Figs. S10-S14.

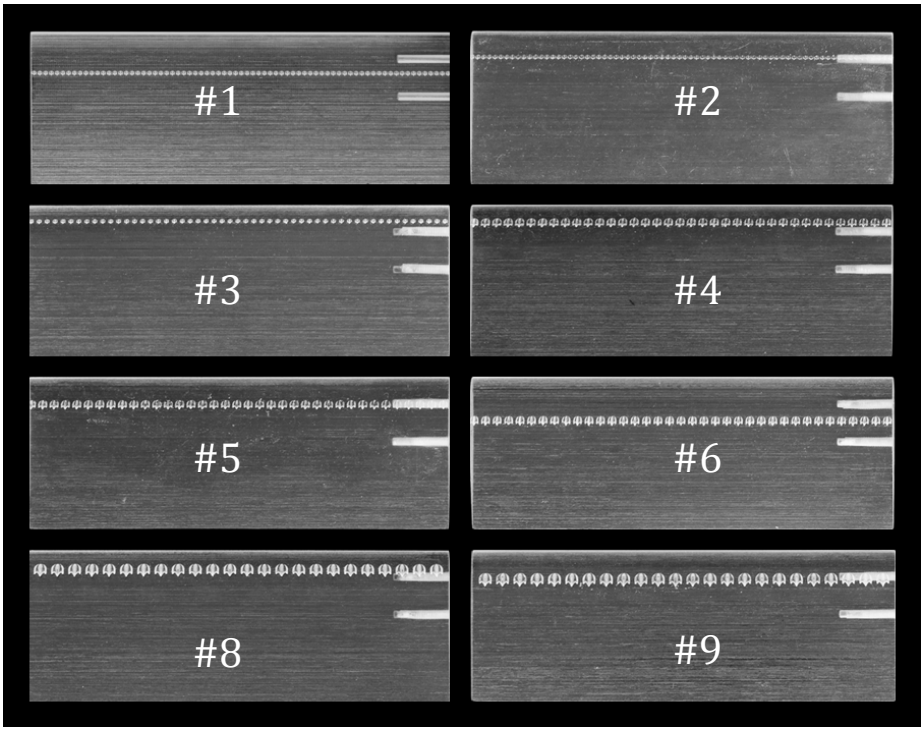

Figure S9: Image of the 8 shark denticle foils comprising a single row of denticles with different chordwise position and denticle size.

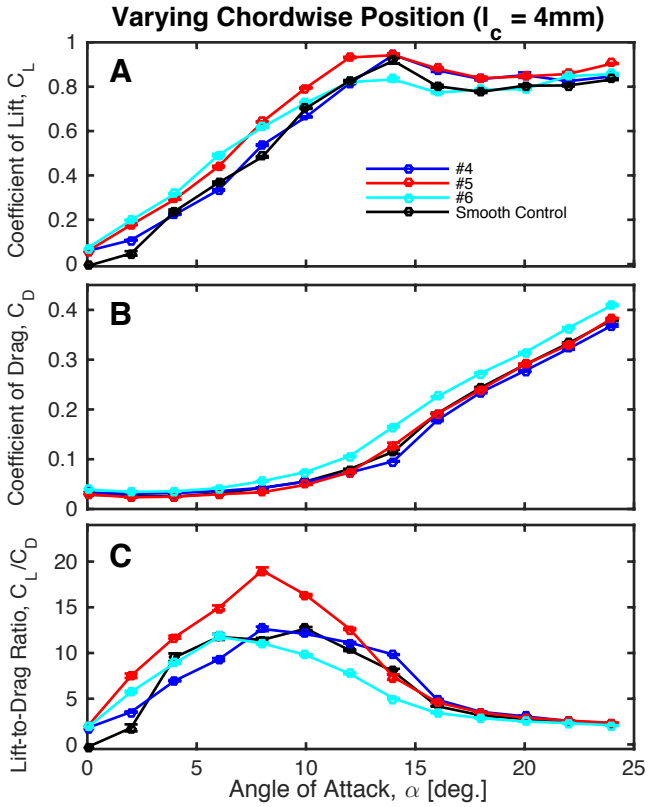

Figure S10: Experimental results for foils #4, #5 and #6. Evolution of (A) lift coefficient, (B) drag coefficient and (C) lift-to-drag ratio as a function of the angle of attack.

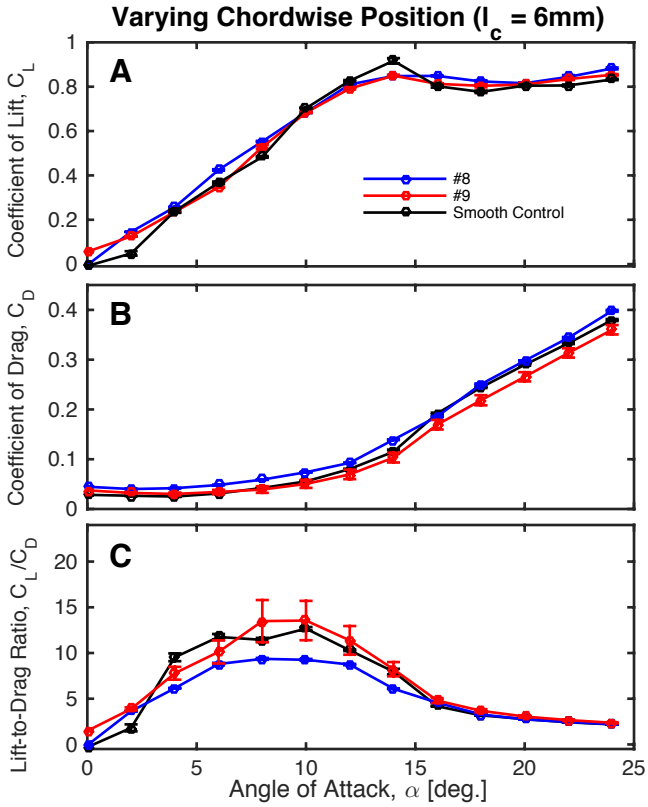

Figure S11: Experimental results for foils #8 and #9. Evolution of (A) lift coefficient, (B) drag coefficient and (C) lift-to-drag ratio as a function of the angle of attack.

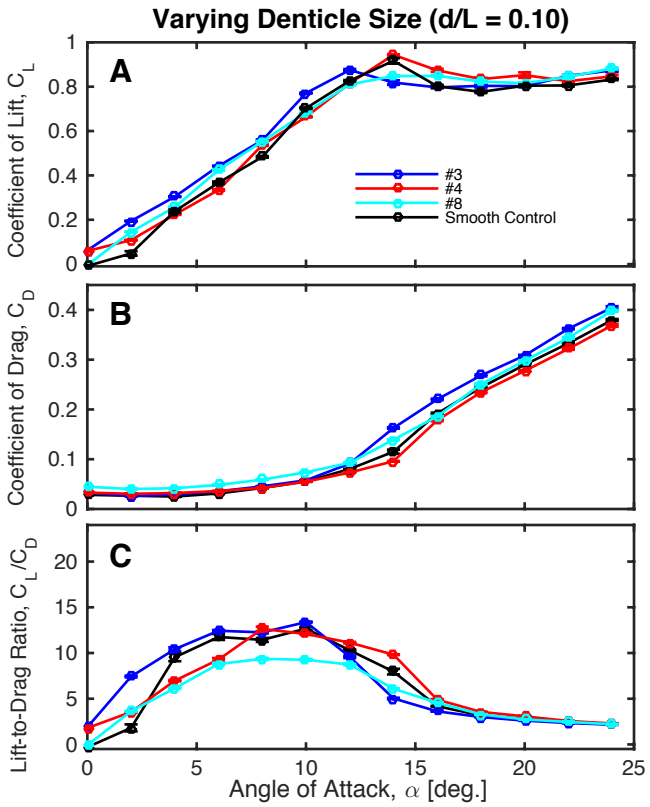

Figure S12: Experimental results for foils #3, #4 and #8. Evolution of (A) lift coefficient, (B) drag coefficient and (C) lift-to-drag ratio as a function of the angle of attack.

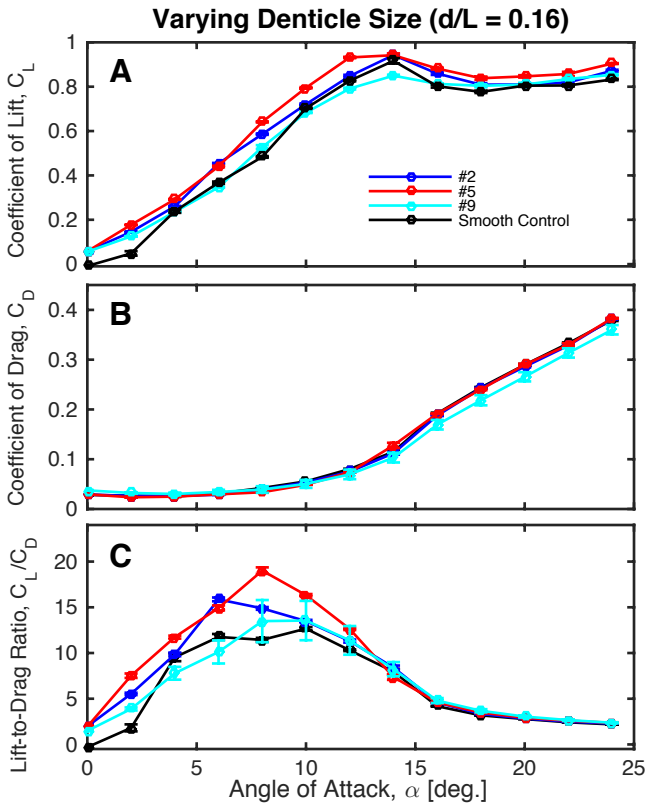

Figure S13: Experimental results for foils #2, #5 and #9. Evolution of (A) lift coefficient, (B) drag coefficient and (C) lift-to-drag ratio as a function of the angle of attack.

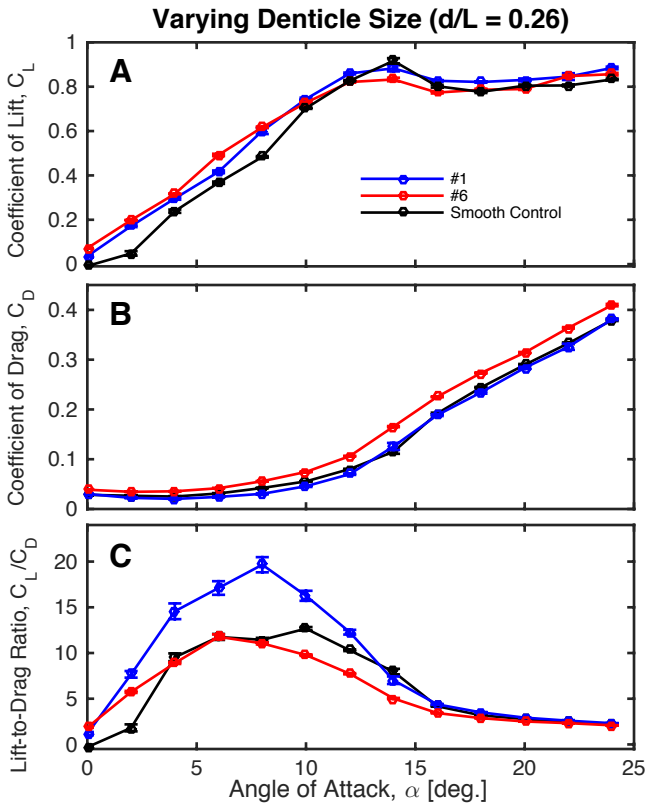

Figure S14: Experimental results for foils #1 and #6. Evolution of (A) lift coefficient, (B) drag coefficient and (C) lift-to-drag ratio as a function of the angle of attack.

S3.2 Varying Chordwise Position for l_c = 2mm

In this section, we consider airfoils with denticles characterized by l_c=2mm, but different chordwise positions (Foils #1-3, #12-13 - see Fig. S15). Data for these foils can be found in Fig. S16.

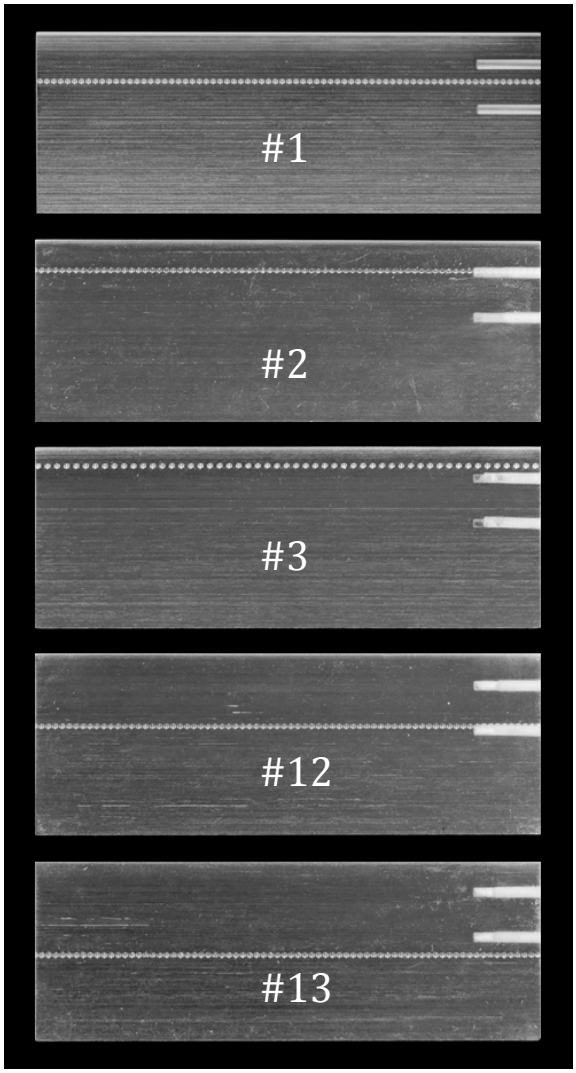

Figure S15: Image of the 5 shark denticle foils comprising a single row of denticles with l_c = 2mm and different chordwise position.

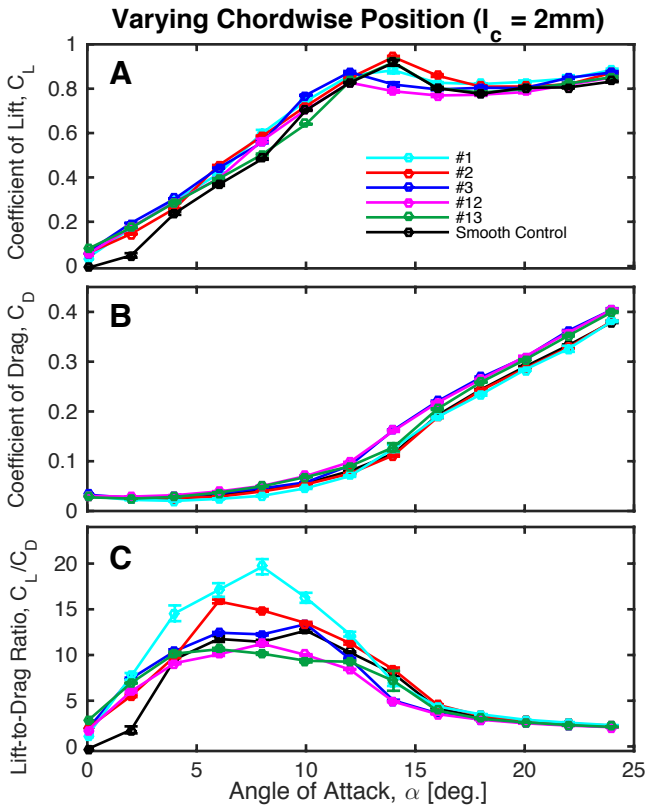

Figure S16: Experimental results for foils #1, #2, #3, #12, and #13. Evolution of (A) lift coefficient, (B) drag coefficient and (C) lift-to-drag ratio as a function of the angle of attack.

S3.3 Varying Tilt Angle of Denticles

In this section, we consider airfoils with a row of denticles characterized by l_c=4mm, but different tilt angles (Foils #5, #7 – see Fig. S17). Data for these foils can be found in Fig. S18.

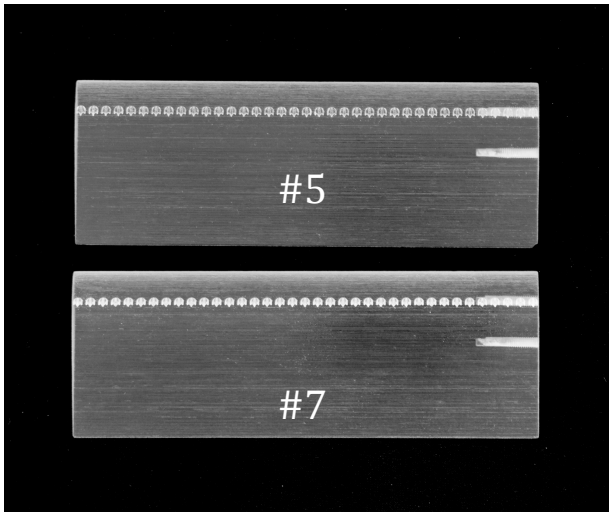

Figure S17: Images of the 2 shark denticle foils comprising a single row of denticles with l_c = 4mm and different tilt angles.

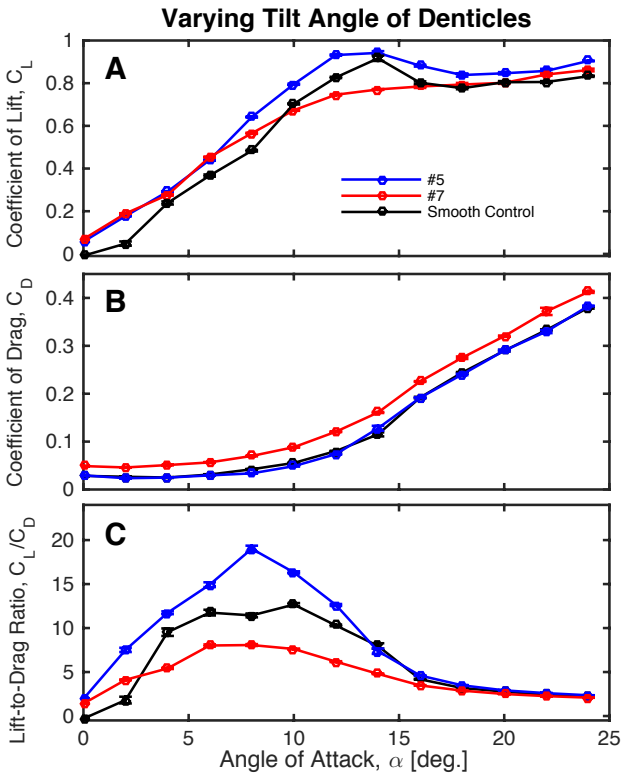

Figure S18: Experimental results for foils #5 and #7. Evolution of (A) lift coefficient, (B) drag coefficient and (C) lift-to-drag ratio as a function of the angle of attack.

S3.4 Varying Spanwise Separation of Denticles

In this section, we consider airfoils with a single row of denticles with l_c=2mm placed at d/L=0.26, but with different spanwise separations between denticles (Foils #1, #10-11 - see Fig. S19). Data for these foils can be found in Fig. S20.

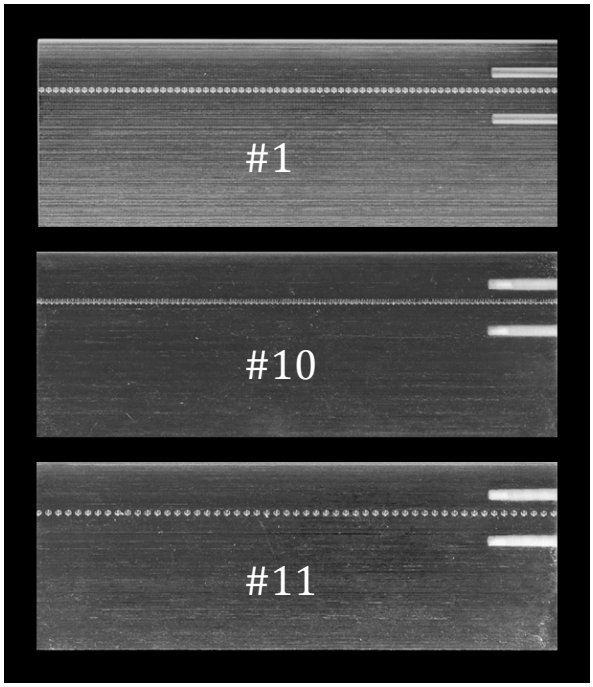

Figure S19: Images of the 3 foils comprising a single row of denticles with l_c=2mm placed at d/L=0.26, but with different spanwise separations.

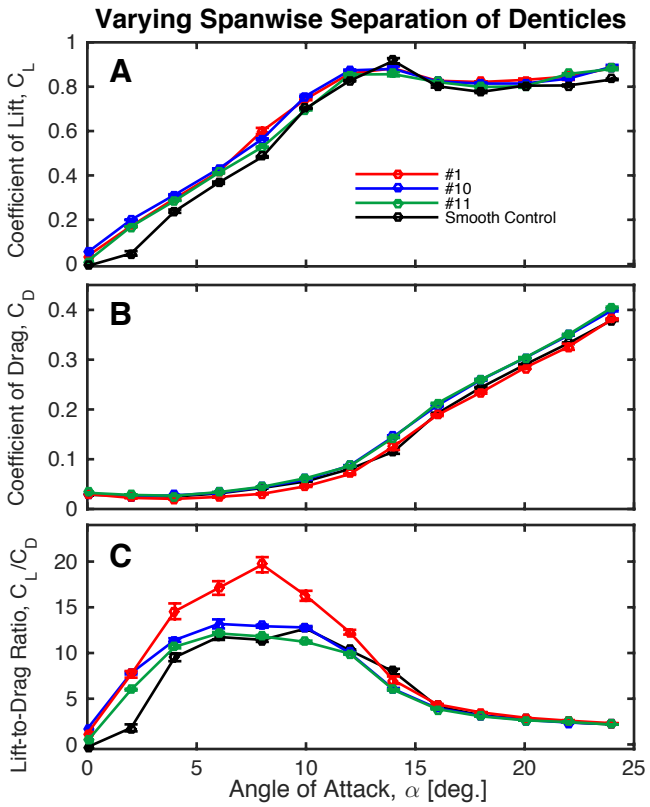

Figure S20: Experimental results for foils #1, #10 and #11. Evolution of (A) lift coefficient, (B) drag coefficient and (C) lift-to-drag ratio as a function of the angle of attack.

S3.5 Varying Chordwise Separation with Two Rows of Denticles

In this section, we consider airfoils comprising two rows of denticles arranged according to the linear pattern with d/L=0.26 with l_c=2mm, but different chordwise separation between rows (Foils #15-17 - see Fig. S2). Data for these foils can be found in Fig. S22.

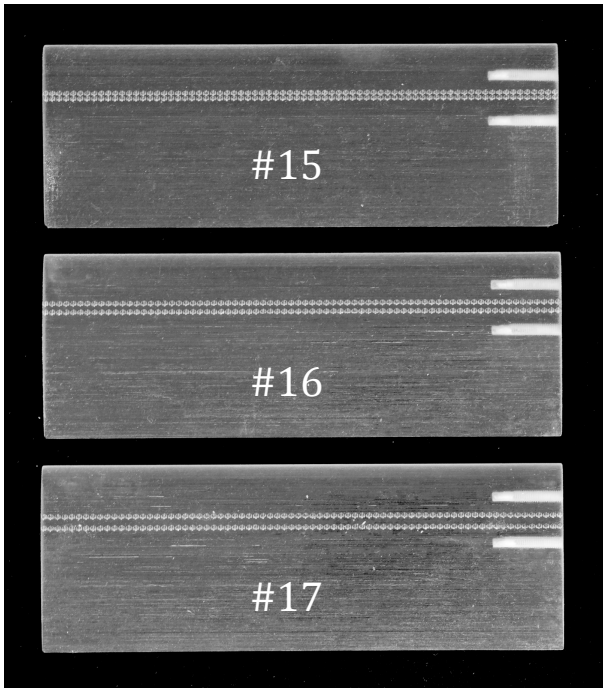

Figure S21: Images of the 3 foils comprising two rows of denticles with different chordwise separation between rows.

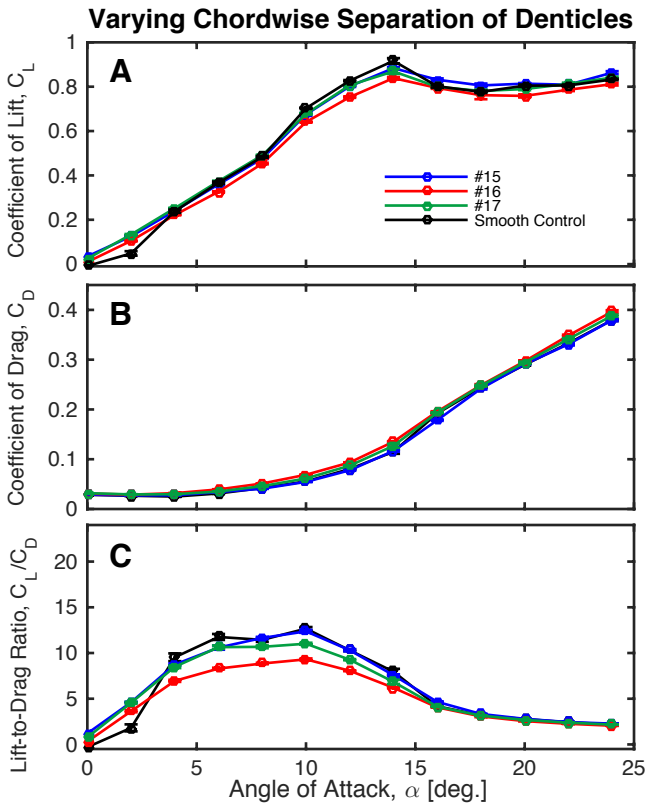

Figure S22: Experimental results for foils #15, #16 and #17. Evolution of (A) lift coefficient, (B) drag coefficient and (C) lift-to-drag ratio as a function of the angle of attack.

S3.6 Varying Pattern with Two Rows of Denticles

In this section, we consider airfoils comprising two rows of denticles with d/L=0.26 and l_c=2mm, but different arrangements (Foils #14-15 - see Fig. S23). Data for these foils can be found in Fig. S24.

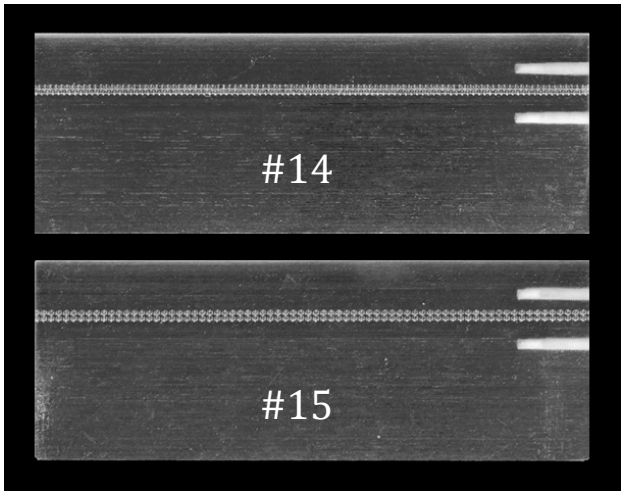

Figure S23: Images of the 2 foils comprising different patterns: staggered (Foil #14) vs. linear (Foil #15).

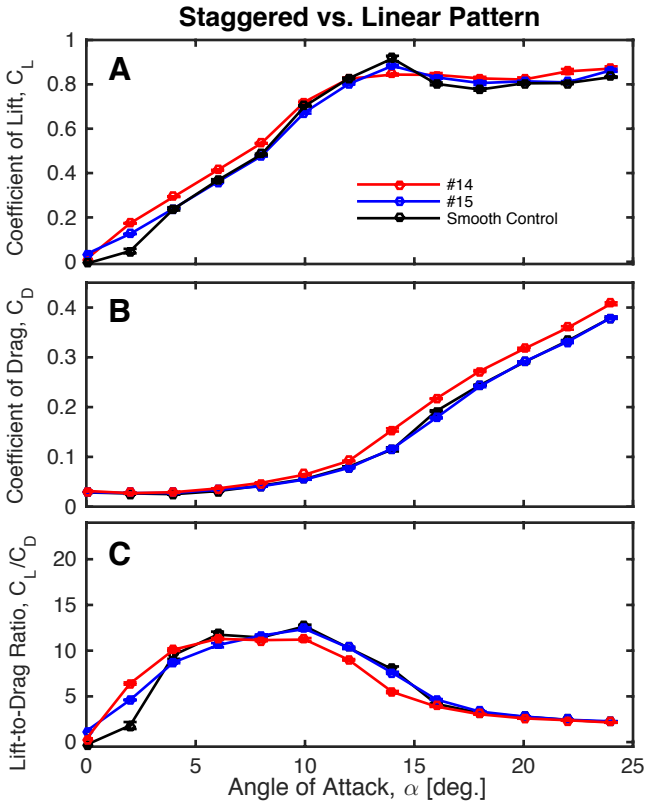

Figure S24: Experimental results for foils #14 and #15. Evolution of (A) lift coefficient, (B) drag coefficient and (C) lift-to-drag ratio as a function of the angle of attack.

S3.7 Foils with 4 or More Rows of Denticles

In this section, we consider airfoils comprising multiple rows (ranging from 4 to 26 rows) of denticles with a variety of different parameters (Foils #18-20 - see Fig. S25). Data for these foils can be found in Fig. S26.

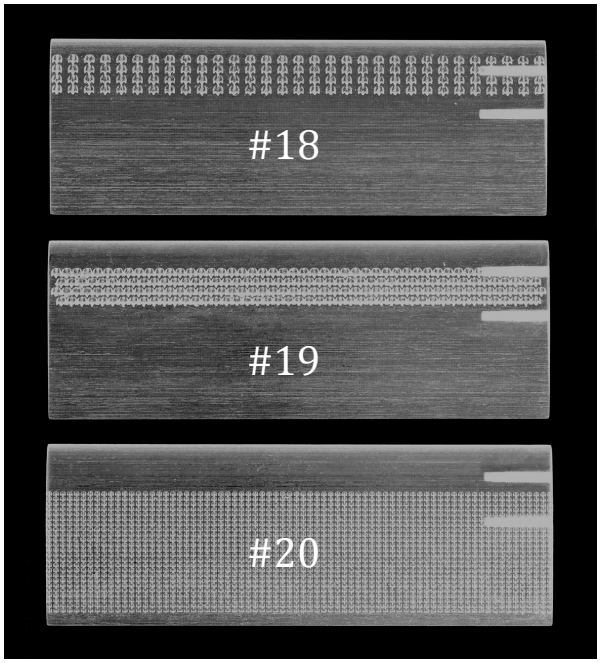

Figure S25: Images of the 3 foils with multiple rows of denticles.

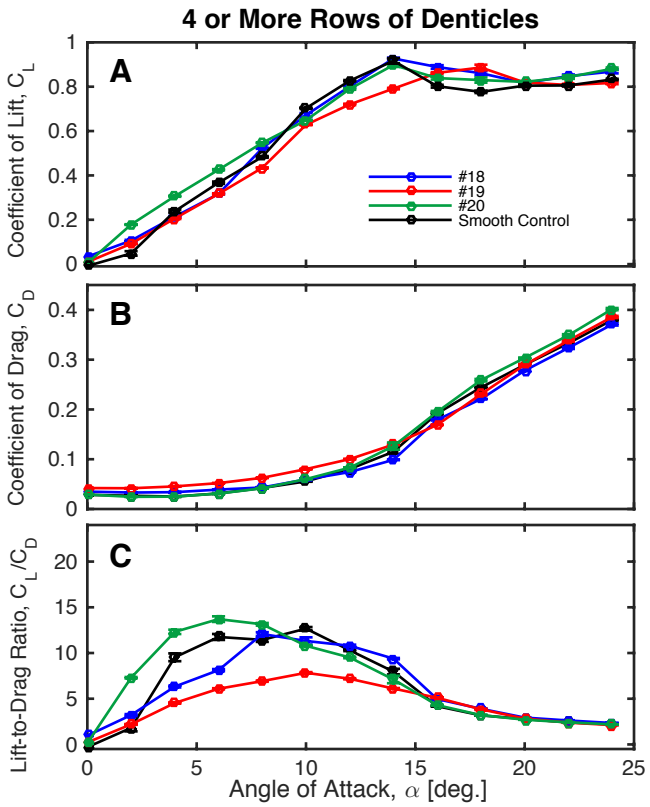

Figure S26: Experimental results for foils #18, #19 and #20. Evolution of (A) lift coefficient, (B) drag coefficient and (C) lift-to-drag ratio as a function of the angle of attack.

S4. Comparison of the Results for the Foils Discussed in the Main Text

In this section, we compare the results of the three foils analyzed in the main text (i.e. best shark denticle, 2D bump profile, and continuous shark-inspired profile foils). Specifically, in Fig. S27 we report the lift-to-drag ratio (L/D) improvement of each of the foils in comparison with the smooth control as a function of angle of attack α. Note that, since the control foil is symmetric and therefore has an L/D of zero at α=0°, the plot begins at α=2°.

The results of Fig. S27 show two key features. First, all three foils provide great improvements in L/D at low angles of attack (i.e. at α=2°), with the shark denticle and continuous shark-inspired profile foils performing significantly better. This is because, although the 2D bump profile enhances lift over twice that of the shark denticle at α=0°, it loses a lot of those lift benefits at higher angles of attack and does not produce a lot of drag reduction since it is not a vortex generator. Second, the continuous shark-inspired profile is outperforming the other two foils at the majority of angles of attack. This is because this profile, which combines aspects of the 2D bump profile and the shark denticle, is able to produce the same lift benefits as the 2D bump at α=0° without losing these lift benefits as much at higher angles of attack (like the 2D bump does), in addition to greatly reducing drag at these higher angles.

In Fig. S27 we also indicate with a filled in marker the angle at which the max L/D occurs for each foil. Note that at this angle the foil can move with its most advantageous lift-to-drag ratio. So for example, if a given application does not have a mandatory angle of attack at which it must move, then this angle of attack would be the most advantageous to use for generating a lot of lift without producing too much drag. We see from Fig. S27 that, like in the case of most angles of attack, the continuous shark-inspired profile produces the greatest improvements at this max L/D (as seen by comparing the filled in markers for each foil).

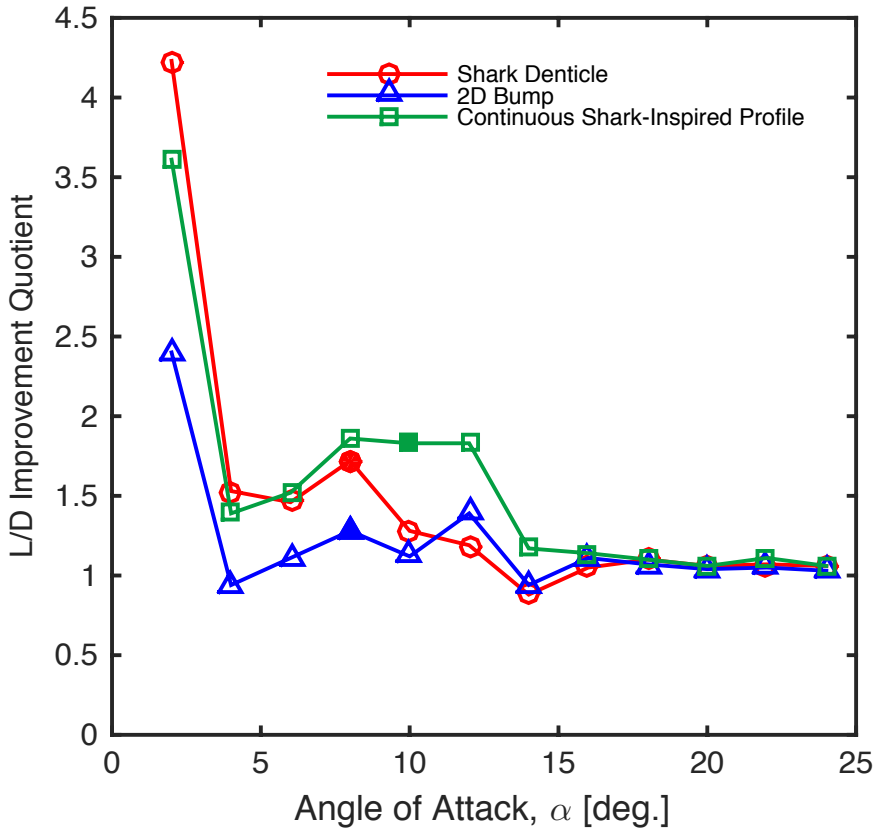

Figure S27: Comparison between the airfoils analyzed in the main text. The red, blue, and green markers correspond to $C_{L/D}^{shark}/C_{L/D}^{control}$, $C_{L/D}^{2Dbump}/C_{L/D}^{control}$, and $C_{L/D}^{cont.}/C_{L/D}^{control}$, respectively. The markers that are filled in represent the angle at which the max L/D for that foil occurs.

S5. Comparison of Shark Skin-Inspired Designs and Traditional Low-Profile Vortex Generators

In this section, we compare the results obtained for the shark skin-inspired designs presented in this study to those of traditional low-profile vortex generator designs. Specifically, we consider the following set of data available in the literature for low-profile vortex generators:

- counter-rotating and co-rotating trapezoid-wing vortex generators arranged on a cambered airfoil. For this system, lift-to-drag ratio measurements as a function of angle of attack at $Re_c \approx 9x10^6$ are reported in Fig. 17 of (9) and Fig. 15 of (10).
- wedge-type vortex generators tested on a "rooftop" section of an airplane wing in transonic flow with M = 0.71. Lift-to-drag ratio measurements as a function of C_L are reported in Fig. 12 of (11).
- co-rotating vane-type vortex generators tested on a "10%-scale configuration of a near-term technology, low-observable, multi-role fighter derivative concept." Lift-to-drag ratio measurements as a function of C_L at a Re≈ 1,300,000 per foot are reported in Fig. 8 of (12).

It is important to note that the vortex generators described above were tested in a much different environment than the study presented here. Although it may be difficult to make a direct comparison, it allows for some reference to the present study.

In Fig. S28 we compare the lift-to-drag ratio (L/D) improvement of our bio-inspired designs (best shark denticle foil and continuous shark-inspired foil) to counter-rotating and co-rotating trapezoid-wing vortex generators described above (9,10), which are the best-reported traditional low-profile VGs as reported in Lin's literature review (13). It appears that on a whole the bio-inspired designs presented here are relatively comparable to the results of these more traditional vortex generators at higher angles of attack near stall and the max L/D. However, the bio-inspired designs presented here show even better improvements at low angles than the traditional low-profile vortex generators. This low angle of attack improvement has potential significance for many systems such as drones, airplanes, and aquatic autonomous vehicles, which can often experience similar low angles of attack in use. Moreover, we see that the continuous shark-inspired profile is producing greater L/D improvements at its max L/D (filled in markers) than any other airfoil is. Once again, this is very beneficial for applications at which the angle of attack is not set, since at this angle the system can move with its most advantageous L/D.

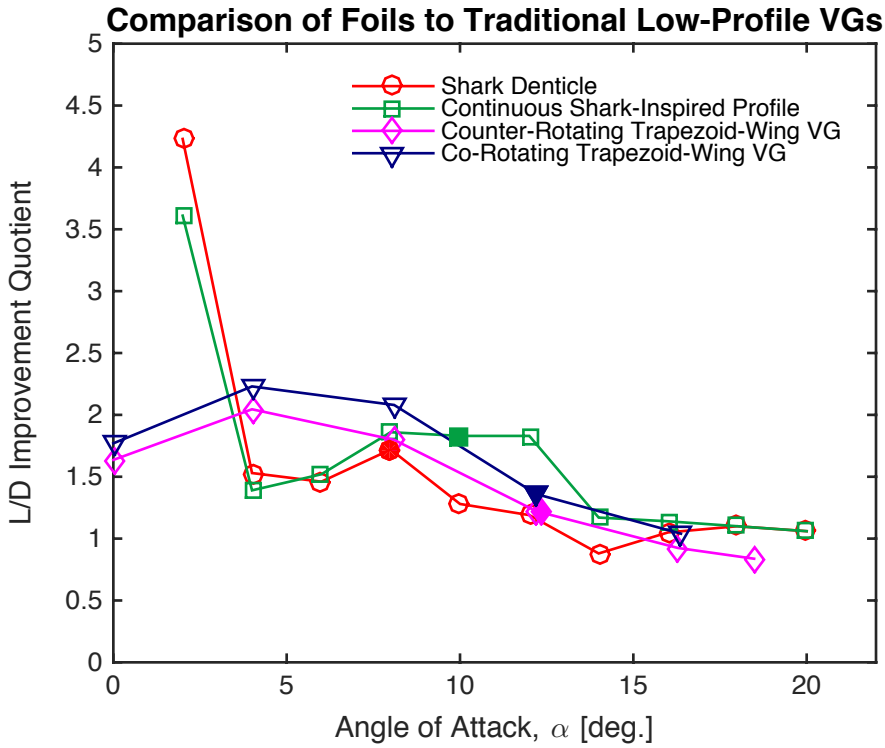

Figure S28: Comparison between the shark skin-inspired designs presented in this study and some of the traditional best low-profile vortex generators reported in the literature. Red, green, magenta, and dark blue markers correspond to $C_{L/D}^{shark}/C_{L/D}^{control}$, $C_{L/D}^{cont.}/C_{L/D}^{control}$, $C_{L/D}^{CTR}/C_{L/D}^{control}$ (CTR denoting counter-rotating trapezoid wing vortex generators), and $C_{L/D}^{COR}/C_{L/D}^{control}$ (COR denoting co-rotating trapezoid wing vortex generators), respectively. The markers that are filled in represent the angle at which the max L/D for that foil occurs.

Finally, in Fig. S29 we compare the lift-to-drag ratio improvements of our best shark skin-inspired designs (best shark denticle foil and continuous shark-inspired profile) to that measured for the wedge-type vortex generators reported in (11) and the co-rotating vane-type vortex generators described in (12). Note that in the plot the L/D improvement is reported as a function of the coefficient of lift, as in (11,12). Analyzing Fig. S29, we find that the shark denticle foil and continuous shark-inspired profile foil show significant improvements compared to the roughly 5% increases that the other studies see. This holds true for all values of C_L tested in these other studies. In addition, just as we saw for the previous two plots, the continuous shark-inspired profile is producing the highest L/D improvements at its max L/D.

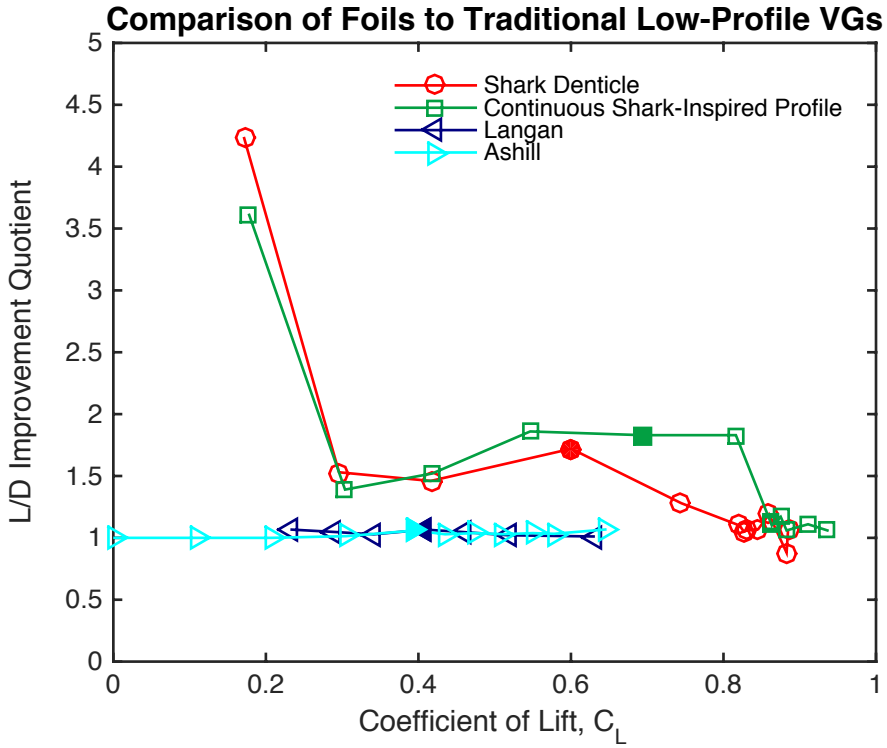

Figure S29: Comparison between the shark skin-inspired designs presented in this study and some of the traditional low-profile vortex generators. Red, green, blue, and cyan markers correspond to $C_{L/D}^{shark}/C_{L/D}^{control}$, $C_{L/D}^{cont.}/C_{L/D}^{control}$, $C_{L/D}^{COR}/C_{L/D}^{control}$ (COR denoting the co-rotating vane-type vortex generators), and $C_{L/D}^{WED}/C_{L/D}^{control}$ (WED denoting the wedge-type vortex generators), respectively. The markers that are filled in represent the angle at which the max L/D for that foil occurs.

S6. CFD Analysis

We used the commercial computational fluid dynamic (CFD) package ANSYS® CFX, release 16.0 to carry out the calculations of flow over the shark denticle design on a flat plate (as discussed in the main text) and the 2D bump foil. This code employs a hybrid finite-volume/finite-element approach to discretize the Navier Stokes equations (14). The equations are solved by an unsteady fully-implicit, fully-coupled multigrid solver in the inertial reference frame of the lab. The Shear Stress Transport (SST) turbulence model (15), which combines the *k-ω* model near the wall and the *k-ε* model away from the wall, is used throughout the study. The choice of turbulence model allows for accurate prediction of onset and amount of flow separation under adverse pressure gradient conditions, and can handle the transition of the flow from laminar to turbulent. The airfoil is placed inside a rectangular fluid domain. An O-type structured mesh is refined around the airfoil and coarsened away from the airfoil. The physical normal distance of the first mesh node above the surface of the airfoil is kept fixed for all the cases. The maximum non-dimensional distance corresponding to the first node above the airfoil surface among all the cases is $y^+ \approx 0.3$. The dimensionless wall distance y^+ is defined as $y^+ = u^* y/\nu$, where u^*, y, and u correspond to the nearest-wall friction velocity, normal distance away from the wall, and kinematic viscosity, respectively.

S6.1 Analysis of 2D Bump Foil

Because of the geometric simplicity of the 2D bump foil compared to the shark denticle foil, 2D simulations of this system were conducted. As done with the experiments, CFD data were computed for angles of attack that extended past stall. For the CFD results shown in Fig. S30, we observe similar results to those seen in the experiments. Positive lift is being generated at zero angle of attack by the 2D bump profile (C_L = 0.22), and we calculate a 946% and 11% increase in lift generated at α=2° and α=4° respectively compared to the control (see Fig. S30*A*). In addition, we notice that lift enhancements by the 2D bump foil are lost at higher angles of attack just as was the case in experiments (see Fig. S30*A*). At low angles of attack, a separation bubble is formed by the 2D bump profile, which leads to separation, and which in turn likely ultimately degrades the performance of the 2D bump foil at higher angles. In regards to drag, it is important to note that at zero angle of attack a very similar drag coefficient is seen in CFD (see Fig. S30*B*) compared to the experiments (both just a bit below 0.03). Because of these lift and drag results, we see an overall qualitatively similar L/D curve as was seen in experiments (see Fig. S30*C*).

Fig. S30*D* shows the CFD streamlines for the 2D bump and control for two low angles of attack at which lift is being enhanced by the 2D bump profile (α=0° and α=4°). Analyzing these images, we see that at 0° a short separation bubble is being generated by the 2D bump foil yet not in the smooth control (as was the case with the shark denticle foil). At 4° we do see a separation bubble developing at the trailing edge of the smooth control. However, this separation bubble is fairly large and does not quite reattach at the trailing edge of the foil, negatively affecting lift. In the 2D bump foil, we see the separation bubble in both CFD and PIV at α=4° much further upstream, which is a more beneficial location in regards to the pressure gradient along the chord as previously discussed.

We should note, however, that there are some differences in the experimental and CFD results, such as the angle at which each of the foils stall and the maximum lift and drag being generated. The 2D CFD calculations here are inherently somewhat different than the 3D experiments which include three-dimensional effects; CFD is a much more idealized version of the experiments. In the experiments, for example, tip vortices may reduce the size of the separation bubble. In spite of some inherent differences between the two, we have shown that there are qualitative similarities between the CFD and experiments, including the following: (*i*) a positive lift enhancement at low angles of attack, (*ii*) non-zero lift at zero angle of attack, and (*iii*) the loss of lift increase relative to the control near and at stall. Furthermore, similar flow mechanisms are seen in both the CFD and PIV streamlines, where short separation bubbles form downstream from the trailing edge of the 2D bump profile.

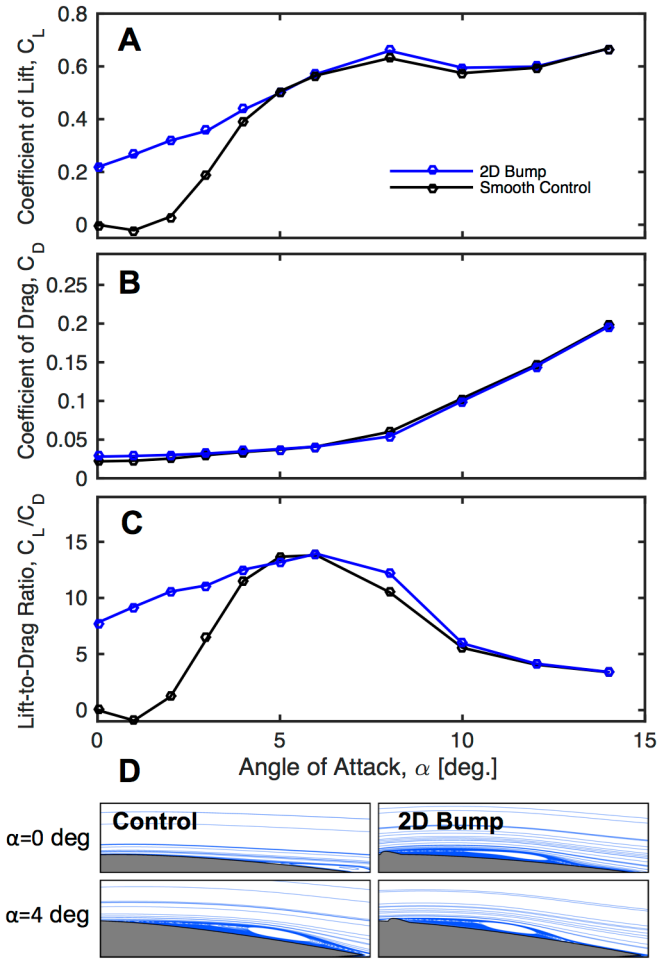

Figure S30: Computational fluid dynamic (CFD) results. Evolution of (A) lift coefficient, (B) drag coefficient and (C) lift-to-drag ratio as a function of the angle of attack. (D) Numerical snapshots showing the streamlines for the control and 2D bump at $\alpha=0^o$ and 4^o.

References

[1] Wen L, Weaver JC, Lauder GV. 2014 Biomimetic shark skin: design, fabrication and hydrodynamic function. *J Exp Biol* **217**, 1656–1666.

[2] Wainwright, D. K. and Lauder, G. V. 2016 Three-dimensional analysis of scale morphology in bluegill sunfish, *Lepomis macrochirus*. *Zoology* **119**, 182-195.

[3] Wainwright, D. K., Lauder, G. V. and Weaver, J. C. 2017 Imaging biological surface topography *in situ* and *in vivo*. *Methods in Ecology and Evolution* doi: 10.1111/2041-210X.12778, in press.

[4] Wen L, Weaver JC, Lauder GV. 2015 Hydrodynamic function of biomemtic shark skin: effect of denticle pattern and spacing. *Bioinspir. Biomim.* 10, 06601.

[5] Lauder GV, et al. 2016 Structure, biomimetics, and fluid dynamics of fish skin surfaces. Physical Review Fluids 1(6). doi:10.1103/physrevfluids.1.060502.

[6] Sadaat, M., Fish, F., Domel, A., Di Santo, V., Lauder, G. V. and H., H.-H. 2017 On the rules for aquatic locomotion. *Physical Review Fluids* in press.

[7] Shelton, R. M., Thornycroft, P. J. M. and Lauder, G. V. 2014 Undulatory locomotion by flexible foils as biomimetic models for understanding fish propulsion. *J. Exp. Biol.* **217**, 2110-2120.

[8] Tank J, Smith L, Spedding GR. 2017 On the possibility (or lack thereof) of agreement between experiment and computation of flows over wings at moderate Reynolds number. *Interface Focus* 7(1):20160076.

[9] Lin JC, Robinson SK, McGhee RJ, Valarezo WO. 1994 Separation control on high-lift airfoils via micro-vortex generators. *J Aircr* **31**, 1317–1323.

[10] Lin J. 1999 Control of turbulent boundary-layer separation using micro-vortex generators. *30th Fluid Dynamics Conference* (American Institute of Aeronautics and Astronautics, Reston, Virigina). doi:10.2514/6.1999-3404.

[11] Ashill P, Fulker J, Hackett K. 2001 Research at DERA on sub boundary layer vortex generators (SBVGs). *39th Aerospace Sciences Meeting and Exhibit* doi:10.2514/6.2001-887.

[12] Langan K, Samuels J. 1995 Experimental investigation of maneuver performance enhancements on an advanced fighter/attack aircraft. 33rd Aerospace Sciences Meeting and Exhibit doi:10.2514/6.1995-442.

[13] Lin JC. 2002 Review of research on low-profile vortex generators to control boundary-layer separation. *Prog Aerosp Sci* 38(4-5):389–420.

[14] ANSYS® Academic Research, Release 14.0, Help System, ANSYS CFX-Solver Theory Guide, ANSYS, Inc.

[15] Menter FR. 1993 Zonal Two Equation k-ω Turbulence Models for Aerodynamic Flows. *AIAA Paper* 93, 2906.